



Loss of phospholipase PLAAT3 causes a mixed lipodystrophic and neurological syndrome due to impaired PPAR γ signaling

Nika Schuermans, Salima El Chehadeh, Dimitri Hemelsoet, Jérémie Gautheron, Marie-Christine Vantyghem, Sonia Nouioua, Meriem Tazir, Corinne Vigouroux, Martine Auclair, Elke Bogaert, et al.

► To cite this version:

Nika Schuermans, Salima El Chehadeh, Dimitri Hemelsoet, Jérémie Gautheron, Marie-Christine Vantyghem, et al.. Loss of phospholipase PLAAT3 causes a mixed lipodystrophic and neurological syndrome due to impaired PPAR γ signaling. *Nature Genetics*, 2023, 55 (11), pp.1929-1940. 10.1038/s41588-023-01535-3 . hal-04385796

HAL Id: hal-04385796

<https://hal.science/hal-04385796>

Submitted on 10 Jan 2024

HAL is a multi-disciplinary open access archive for the deposit and dissemination of scientific research documents, whether they are published or not. The documents may come from teaching and research institutions in France or abroad, or from public or private research centers.

L'archive ouverte pluridisciplinaire **HAL**, est destinée au dépôt et à la diffusion de documents scientifiques de niveau recherche, publiés ou non, émanant des établissements d'enseignement et de recherche français ou étrangers, des laboratoires publics ou privés.

Loss of phospholipase PLAAT3 causes a mixed lipodystrophic and neurological syndrome due to impaired PPAR γ signaling

Nika Schuermans,^{1,2,31} Salima El Chehadeh,^{3,4,5,31} Dimitri Hemelsoet,^{6,31} Jérémie Gautheron,^{7,31} Marie-Christine Vantyghem,^{8,9} Sonia Nouioua,^{10,11} Meriem Tazir,^{11,12} Corinne Vigouroux,^{7,13} Martine Auclair,^{7,13} Elke Bogaert,^{1,2} Sara Dufour,^{2,14,15} Fumiya Okawa,¹⁶ Pascale Hilbert,¹⁷ Nike Van Doninck,¹⁸ Marie-Caroline Taquet,¹⁹ Toon Rosseel,¹ Griet De Clercq,^{1,2} Elke Debackere,^{1,2} Carole Van Haverbeke,²⁰ Ferroudja Ramdane Cherif,^{10,11} Jon Andoni Urtizberea,²¹ Jean-Baptiste Chanson,²² Benoit Funalot,^{23,24} François-Jérôme Authier,^{24,25} Sabine Kaya,²⁶ Wim Terry,²⁷ Steven Callens,²⁸ Bernard Depypere,²⁹ Jo Van Dorpe,²⁰ Program for Undiagnosed Diseases (UD-ProZA), Bruce Poppe,^{1,2} Francis Impens,^{2,14,15} Noboru Mizushima,¹⁶ Christel Depienne,^{4,26} Isabelle Jéru,^{7,30,32} Bart Dermaut.^{1,2,32,*}

¹Center for Medical Genetics, Ghent University Hospital, Ghent, 9000, Belgium

²Department of Biomolecular Medicine, Faculty of Medicine and Health Sciences, Ghent University, Ghent, 9000, Belgium

³Service de Génétique Médicale, Institut de Génétique Médicale d'Alsace (IGMA), Hôpitaux Universitaires de Strasbourg, Strasbourg, France

⁴Institut de Génétique et de Biologie Moléculaire et Cellulaire (IGBMC), INSERM U1258, CNRS-UMR7104, Université de Strasbourg, Illkirch- Graffenstaden, France

⁵Laboratoire de Génétique Médicale, UMRS_1112, Institut de Génétique Médicale d'Alsace (IGMA), Université de Strasbourg et INSERM, Strasbourg, France

⁶Department of Neurology, Ghent University Hospital, Ghent, 9000, Belgium

⁷Sorbonne Université, Inserm UMRS_938, Centre de Recherche Saint-Antoine (CRSA), Paris 75012, France

⁸Endocrinology, diabetology, metabolism department, National Competence Centre for Rare Diseases of Insulin Secretion and Insulin Sensitivity (PRISIS), Lille University hospital, Lille, 59 000, France

⁹University of Lille, INSERM U1190, European Genomic Institute for Diabetes, Lille, 59 000, France

¹⁰Department of Neurology of the EHS of Cherchell, Tipaza, Algeria

¹¹NeuroSciences Research Laboratory, University of Algiers Benyoucef Benkhedda, Algiers, Algeria

¹²Department of Neurology, CHU Algiers (Mustapha Pacha Hospital), Algiers, Algeria

¹³Assistance Publique-Hôpitaux de Paris, Saint-Antoine University Hospital, National
 Reference Center for Rare Diseases of Insulin Secretion and Insulin Sensitivity (PRISIS),
 Department of Endocrinology, Diabetology and Reproductive Endocrinology, and
 Department of Molecular Biology and Genetics, Paris, France
¹⁴VIB-UGent Center for Medical Biotechnology, VIB, Ghent, Belgium
¹⁵VIB Proteomics Core, VIB, Ghent, Belgium.
¹⁶Department of Biochemistry and Molecular Biology, Graduate School and Faculty of
 Medicine, The University of Tokyo, Japan
¹⁷Institute of Pathology and Genetics, Department of Molecular and Cellular Biology,
 Charleroi, 6041, Belgium
¹⁸General Hospital VITAZ, Department of Endocrinology and Diabetology, Sint-Niklaas,
 9100, Belgium
¹⁹Department of Internal Medicine and Nutrition, Hopitaux Universitaires Strasbourg,
 Strasbourg, 67000, France
²⁰Department of Pathology, Ghent University Hospital, Ghent, 9000, Belgium
²¹Institut de Myologie, Paris, France
²²Service de neurologie et centre de référence neuromusculaire Nord/Est/Ile de France,
 Hôpital de Haute-pierre, Strasbourg, 67000, France
²³Department of Medical Genetics, Hôpital Henri Mondor, Université Paris-Est-Créteil,
 Créteil, 94010, France
²⁴Inserm UMR955, Team Relaix, Faculty of Medicine, Créteil, 94010, France
²⁵Centre Expert de Pathologie Neuromusculaire/Histologie, Département de Pathologie,
 Hôpital Henri Mondor, Université Paris-Est-Créteil, Créteil, 94010, France
²⁶Institut für Humangenetik, Universitätsklinikum Essen, Essen, 45147, Germany
²⁷Department of Nephrology, Jan Yperman Hospital, Ieper, 8900, Belgium
²⁸Department of General Internal Medicine, Ghent University Hospital, Ghent, 9000, Belgium
²⁹Department of Plastic and Reconstructive Surgery, Ghent University Hospital, Ghent, 9000
 Belgium
³⁰Sorbonne Université, AP-HP, Pitié-Salpêtrière Hospital, Department of Medical Genetics,
 DMU BioGeM; Paris, France
³¹These authors contributed equally
³²These authors jointly supervised this work
 *Correspondence: bart.dermaut@ugent.be

69 **Abstract**

70 PLAAT3 is a phospholipid-modifying enzyme predominantly expressed in neural and white
71 adipose tissue (WAT). It is a potential drug target for metabolic syndrome, as *Plaat3* deficiency
72 in mice protects against diet-induced obesity. We identified seven patients from four unrelated
73 consanguineous families, with homozygous loss-of-function variants in *PLAAT3*, who
74 presented with a lipodystrophy syndrome with loss of fat varying from partial to generalized
75 and associated with metabolic complications, as well as variable neurological features including
76 demyelinating neuropathy and intellectual disability. Multi-omics analysis of mouse *Plaat3*^{-/-}
77 and patient-derived WAT showed enrichment of arachidonic acid-containing membrane
78 phospholipids and a strong decrease in the signaling of PPAR γ , the master regulator of
79 adipocyte differentiation. Accordingly, CRISPR/Cas9-mediated *PLAAT3* inactivation in human
80 adipose stem cells induced insulin resistance, altered adipocyte differentiation with decreased
81 lipid droplet formation and reduced the expression of adipogenic and mature adipocyte markers,
82 including PPAR γ . These findings establish PLAAT3 deficiency as a hereditary lipodystrophy
83 syndrome with neurological manifestations, caused by a PPAR γ -dependent defect in WAT
84 differentiation and function.

85 **MAIN**

86 Human PLAAT3, previously known as phospholipase A2, group XVI (PLA2G16), is part of a
87 family of acyltransferases and phospholipases, which catalyze phospholipase A (PLA) and
88 acyltransferase (AT) activities.⁽¹⁾ In mice, *Plaat3* is highly expressed in white adipose tissue
89 (WAT) where it exhibits PLA₁ and PLA₂ activities, which hydrolyze fatty acids linked to the
90 *sn-1* or *sn-2* positions of membrane phospholipids.⁽¹⁻⁴⁾ *Plaat3*-deficient mice are resistant to
91 diet-induced obesity, and PLAAT3 was therefore suggested as a potential therapeutic target for
92 metabolic syndrome.⁽⁵⁾

93 Lipodystrophy syndrome is characterized by generalized or partial lipoatrophy with
94 reduced WAT due to a defect in adipose tissue storage of triglycerides (TG).⁽⁶⁾ This results in
95 lipid infiltration of non-adipose tissues leading to insulin resistance, increased liver glucose
96 production, hypertriglyceridemia, and hepatosteatosis. Approximately 30 genes have been
97 implicated in hereditary lipodystrophy syndrome.^(7, 8) Although these disorders often remain
98 genetically unexplained, there is growing interest in identifying their molecular bases to
99 improve genetic counseling, personalize treatment,^(9, 10) and uncover signaling pathways
100 involved in diabetes, hepatosteatosis, or metabolic syndrome.^(9, 10) Patients with lipodystrophy
101 syndrome show striking metabolic similarities with obese subjects who display an incapacity
102 to store surplus energy in overwhelmed WAT resulting in ectopic lipid accumulation.

103 In this study, we combined homozygosity mapping, whole-exome and whole-genome
104 sequencing (WES/WGS) to identify homozygous null variants in *PLAAT3* as a cause of
105 lipodystrophy syndrome with neurological features. We further assessed the metabolic
106 consequences of the loss of PLAAT3 using a multi-omics approach in murine and human WAT.
107 The impact of the loss of PLAAT3 activity on human adipocyte differentiation and function
108 was also evaluated using a CRISPR-Cas9-mediated genome-editing approach.

109

110 **RESULTS**

111 **Identification of homozygous *PLAAT3* null variants in seven patients**

112 In a consanguineous family with three children (patients 1-3; family 1) (Figure 1a) presenting
113 with a lipodystrophy syndrome combining metabolic and neurological manifestations, we
114 performed SNP array-based homozygosity mapping in the three affected and two unaffected
115 siblings. The largest homozygous region (~43 Mb), exclusively shared between the affected
116 siblings, was found on chromosome 11p11.2-q14.2 and contained the *BSCL2* gene, implicated

in congenital generalized lipodystrophy type 2 (CGL2) (Supplementary Table 1). Normal Sanger sequencing of *BSCL2* coding exons, followed by normal cDNA analysis of peripheral leukocytes, excluded *BSCL2* as the causal gene. WES was performed in the three affected sisters and two unaffected siblings, but we found no homozygous pathogenic single nucleotide variants in the region of interest (Supplementary Table 2). Copy number variant analysis of WES data using ExomeDepth⁽¹¹⁾ revealed a homozygous 103 bp deletion corresponding to exon 2 of the *PLAAT3* gene (NM_001128203.2) exclusively in the three affected sisters (Figure 1b (upper panel), Supplementary Table 3). The deletion was located within the ~43 Mb shared homozygous region and was confirmed by low-pass whole genome sequencing (CNV-seq).⁽¹²⁾ WGS in one unaffected and two affected sisters determined the genomic deletion breakpoints (chr11: 63597894-63602986) revealing a homozygous 5092 bp deletion (Figure 1b (lower panel)). Deletion of *PLAAT3* exon 2 (c.16-4823_118+167del) results in a frameshift leading to a premature termination codon (p.(Pro6ValfsTer15)) (Figure 1c). RNA sequencing confirmed that the molecular defect induced nonsense-mediated decay (NMD) (Supplementary Figure 1).

Using the GeneMatcher platform,⁽¹³⁾ we identified a female patient (patient 4; family 2) (Figure 1a) in whom WES revealed a homozygous single base duplication in exon 3 of *PLAAT3* leading to a frameshift and premature termination codon, predicted to induce NMD (c.286dupG, p.(Ala96GlyfsTer16)) (Figures 1b, c).⁽¹³⁾ Through data sharing we found three additional patients from two unrelated families (patient 5; family 3, patients 6-7; family 4) (Figure 1a) in which WES identified a homozygous nonsense variant (c.339C>A; p.(Cys113Ter)) in exon 3 of *PLAAT3* (Figure 1c). The variants identified in families 2, 3 and 4 were confirmed by Sanger sequencing (Figure 1b). Only the p.(Cys113Ter) variant was present in gnomAD v3.1.2 (in one individual of African origin in the heterozygous state).

Loss of PLAAT3 is associated with a lipodystrophy syndrome

Family 1. Three sisters (patients 1-3), born from consanguineous parents of Turkish origin, presented with lipoatrophy of limbs and trunk and lipohypertrophy in the submental and posterior cervical region in patients 2 and 3 (Figure 1a). The patients were lean with a body-mass index (BMI) ranging from 19.6 to 20.5 kg/m². In patient 1 the lipoatrophy was confirmed by dual X-ray absorptiometry with a total fat mass of 13.8% (Figure 2a). Serum leptin levels in patient 1 and patient 2 were decreased (Supplementary Table 4). Other clinical signs typical for lipodystrophy syndrome included muscle hypertrophy, insulin-resistant diabetes with hyperinsulinemia, *acanthosis nigricans* and increased fasting glucose, hypertriglyceridemia with low HDL-cholesterol, liver steatosis, and polycystic ovary syndrome with hirsutism

(Figure 2b, Table 1, Supplementary Table 4). Neurological symptoms comprised migraine (patient 1), demyelinating neuropathy (patient 1) and intellectual disability (patient 2) (Table 1, Supplementary Table 4). Patient 1 presented with unilateral carpal tunnel syndrome. Additional features included generalized musculoskeletal pain, hypertension, subclinical hypothyroidism, precocious puberty and acromegalic features (Supplementary Table 4). Short stature was seen in all three affected siblings, which was probably constitutional given the short stature in both unaffected parents (mother: 158 cm, father: 165 cm).

Family 2. Patient 4 (female) was born from Algerian first-degree cousins (Figure 1a). She presented with an android habitus with generalized muscle hypertrophy and lipoatrophy in the limbs with a relative accumulation of adipose tissue in the face, neck and submental region resulting in a cushingoid appearance (Figure 2c). She had a BMI of 24.6 kg/m² with insulin-resistant diabetes, hypertriglyceridemia with low HDL-cholesterol, liver steatosis, polycystic ovary syndrome and hirsutism. She complained of chronic muscle pain and was diagnosed with demyelinating neuropathy (Table 1). Arterial hypertension, transient hypothyroidism, carpal tunnel syndrome, obstructive sleep apnea syndrome and glomerulopathy without renal insufficiency were observed (Supplementary Table 4). Recently, she was diagnosed with thyroid vesicular carcinoma requiring thyroidectomy.

Family 3. Patient 5 (male) was born from Algerian first-degree cousins (Figure 1a). His mother had two early miscarriages before his birth. He presented with generalized lipodystrophy, muscular hypertrophy, insulin-resistant diabetes, and liver steatosis (Figure 2d, Table 1). The patient was lean with a BMI of 20.7 kg/m² and a body fat percentage of 10.1% (Table 1, Supplementary Table 4). Serum leptin levels were very low. He developed gynecomastia at the age of 12 years, which persisted after puberty (Figures 2d, e). Sex hormone levels were normal, with slightly elevated free testosterone levels due to decreased sex hormone binding globulin (SHBG) levels associated with insulin resistance. LH was within the normal range, FSH was slightly upregulated with low inhibin B levels, suggesting spermatogenic insufficiency (Supplementary Table 4). He presented with facial dysmorphism including low-set and posteriorly rotated ears, prominent nose and forehead, high nasal bridge and prognathism. Musculoskeletal manifestations included thoracic hyperkyphosis, *genu valgum*, *talipes equinovarus*, retraction of Achilles tendons, hammer toes and bilateral syndactyly of the second and third toes (Figures 2d-g). The patient presented with a rather short stature which was also seen in his unaffected parents (Supplementary Table 4). During childhood, advanced bone age with bone hypermineralization (Z-score >3.5 SD) was observed. Neurological features

consisted of psychomotor delay, intellectual disability, behavioral problems, demyelinating neuropathy and spastic gait (Table 1). MRI of the brain was normal.

Family 4. Patients 6 and 7 (male brothers) were born from Algerian first-degree cousins (Figure 1a). They were lean with normal BMIs and displayed facial acromegalic features, kyphoscoliosis, and lumbar hyperlordosis (Table 1). Both patients presented with walking difficulties at the age of 4 years. Neuromusculoskeletal manifestations included tiptoe walking, absence of deep tendon reflexes, retraction of Achilles tendons and muscle pain. Metabolic features included partial lipoatrophy affecting the shoulder girdle, upper extremities and trunk associated with muscular hypertrophy and pronounced subcutaneous veins, gynecomastia, insulin resistance, acanthosis nigricans, diabetes, liver steatosis, hypertriglyceridemia in the older brother and decreased HDL cholesterol in the younger brother (Figures h, i, Table 1, Supplementary Table 4). Development of secondary sex characteristics was normal, reflected by normal gonadotropin and sex hormone levels (Supplementary Table 4). A demyelinating sensorimotor neuropathy was present in both patients. Brain-MRI revealed Arnold-Chiari malformation type 1 in patient 6 (Supplementary Table 4).

***Plaat3*^{-/-} mouse WAT displays a PPAR γ -dependent differentiation defect**

The mouse *Plaat3* protein is evolutionary highly conserved and is 83% identical and 91% similar to human PLAAT3 (<https://www.flyrnai.org/diopt>). *Plaat3*^{-/-} mice have been reported to be resistant to diet-induced obesity and show a lipodystrophy syndrome-like phenotype.⁽⁵⁾ This phenotype was suggested to be due to loss of PLA₂ activity resulting in a decline in arachidonic acid (AA, C20:4) release and prostaglandin E₂ (PGE₂) synthesis and an increase in levels of cAMP, leading to increased lipolysis in normally differentiated adipocytes.⁽⁵⁾ Other studies have suggested an important role for PLAAT3 in adipocyte differentiation.⁽¹⁴⁻¹⁶⁾

We used *Plaat3*^{-/-} mice-derived inguinal WAT samples⁽¹⁷⁾ for morphological and multi-omics studies to further clarify the pathogenic mechanism of PLAAT3-related lipodystrophy syndrome. We collected 12 inguinal *Plaat3*^{-/-} WAT biopsy specimens and 12 *Plaat3*^{+/-} inguinal WAT control specimens. Light microscopic analysis of *Plaat3*^{-/-} samples and *Plaat3*^{+/-} controls showed that adipocytes in *Plaat3*-deficient tissue were significantly smaller in size, in line with a previous report⁽⁵⁾, while no difference in shape ('circularity') was observed (Figures 3a, b).

Next, we evaluated the effect of *Plaat3* deficiency on the lipid content in inguinal WAT using a liquid chromatography-tandem mass spectrometry (LC-MS/MS) lipidomics approach. Dimensionality reduction showed clustering of samples according to sex along the first component and according to genotype (*Plaat3*^{-/-} or *Plaat3*^{+/-}) along the second component,

indicating that loss of *Plaat3* activity influences the abundance of certain lipid classes and species (Figure 3c). Given the known enzymatic function of PLAAT3 in membrane phospholipid remodeling, we checked the overall abundance of the 11 phospholipid subclasses in *Plaat3*^{+/-} and *Plaat3*^{-/-} WAT (Supplementary Figure 2). Increased levels were seen for phosphatidylethanolamine (PE), phosphatidylinositol (PI), phosphatidylserine (PS) and 1-alkenyl, 2-acyl phosphatidylethanolamine (PE-P) in both female and male *Plaat3*^{-/-} WAT, with PI and PS showing the most striking differences (Supplementary Figure 2). Within each phospholipid subclass we filtered all phospholipid species with statistically significant ($p < 0.05$) differences between *Plaat3*^{+/-} and *Plaat3*^{-/-} WAT that showed alterations in the same direction in female and male samples. This revealed a total of 14 lipid species (Supplementary Table 5) of which two, PI(18:0/20:4) and PE(18:0/18:2), represent the most common species within their lipid class and were clearly upregulated in *Plaat3*^{-/-} WAT (Plaat3 mouse lipidomics.html). In animal tissues, PI(18:0/20:4) is the primary source of AA (C20:4) required for biosynthesis of eicosanoids (including prostaglandins) via PLA₂ activity, which releases these bioactive fatty acids from position *sn*-2.⁽¹⁸⁾ However, mediator lipidomics showed no statistically significant differences for AA or AA-derived eicosanoids, including PGE₂, between *Plaat3*^{-/-} and *Plaat3*^{+/-} WAT (Figure 3d) (Plaat3 mouse mediator lipidomics.html).

We also performed RNA sequencing on seven *Plaat3*^{-/-} (3 male, 4 female) and eight *Plaat3*^{+/-} mouse (4 male, 4 female) WAT samples. A total of 99 genes were significantly differentially expressed ($|\log_2FC| \geq 1$, raw $p < 0.05$), of which 59 were upregulated and 40 downregulated (Figure 3e). We used Metascape to search for enriched pathways within the differentially expressed gene sets (top 100 down- and upregulated genes ranked by FC with raw p -values < 0.05) and found that genes involved in synaptic transmission, glycolipid biosynthetic processes and fat cell differentiation were downregulated, whereas genes involved in myelination and inflammatory responses were upregulated in *Plaat3*^{-/-} WAT (Figure 3f). We used the LISA tool to identify transcriptional regulators (TRs) of gene networks within the down- and upregulated genes (Figure 3g).⁽¹⁹⁾ Interestingly, the most important TR of the downregulated genes was peroxisome proliferator activated receptor gamma (PPARG or PPAR γ), which is responsible for adipocyte differentiation together with its coactivator retinoid X receptor alpha (RXRA or RXR α) with which it forms a heterodimer to induce transcription of target genes.^(20, 21) Transcript levels of the three lipolytic enzymes (*Pnpla2*, *Lipe* and *Mgll*) were not altered in *Plaat3*^{-/-} WAT compared to *Plaat3*^{+/-} (Supplementary Figure 3).

Finally, LC-MS/MS-based shotgun proteomics analysis was performed on 9 *Plaat3*^{-/-} (4 males, 5 females) and 9 *Plaat3*^{+/-} (4 males, 5 females) inguinal WAT biopsy specimens which

reliably quantified a total of 4033 protein groups in all samples. Differential protein intensity analysis ($|\log_2FC| \geq 0.5$, raw $p < 0.05$) showed 41 significantly downregulated and 8 upregulated proteins (Figure 3h). Again, we looked for enriched pathways within the top 100 down- and upregulated proteins (ranked according to FC with raw p -value < 0.05). Proteins involved in fatty acid metabolic and lipid biosynthetic processes were less abundant in *Plaat3*^{-/-} WAT, whereas proteins involved in autophagy and catabolism were more abundant (Figure 3i). With the LISA tool, PPAR γ and its coactivators, such as CCAAT enhancer binding protein alpha and beta (CEBPA and CEBPB), were again identified as the strongest TRs within the set of downregulated proteins (Figure 3j). The most strongly upregulated protein was Plin2 ($|\log_2FC| = 2.69$, raw $p < 0.0001$) (Figure 3h). PLIN2 is known to be expressed on lipid droplet membranes of preadipocytes and is replaced by PLIN1 after completion of the cell maturation process.⁽²²⁾ Along with PLIN3, PLIN2 also contributes to the formation of lipid droplet-lysosome contacts and their removal by chaperone-mediated autophagy facilitates lipolysis.^(23, 24) Taken together, these results show that mouse *Plaat3*^{-/-} WAT consists of smaller adipocytes containing increased levels of the PI(18:0/20:4) membrane phospholipid and showing a PPAR γ -dependent adipocyte differentiation defect with abnormal lipid droplet metabolism.

Patient WAT shows a PPAR γ -mediated adipogenesis defect

We collected subcutaneous WAT samples of female patients 1 and 4, as well as six healthy female controls with a normal BMI (19-23 kg/m²). Light microscopic analysis showed that patient adipocytes were larger and showed a statistically significant difference in ‘circularity’ (Figures 4a, b). Patient WAT also displayed increased inflammation as assessed by CD68 staining (Figure 4a (middle panels)). Immunohistochemistry using a PMP70 (70-kDa peroxisomal membrane protein) antibody did not show remarkable differences in peroxisome abundance (Figure 4a (right panels)).

LC-MS/MS-based lipidomics analysis was performed on the two patient WAT samples and six controls. Principal component analysis (PCA) based on all the measured lipid species across all classes showed that the lipid profile in the patients clearly differed from that in the controls (Figure 4c). We again focused on phospholipids and observed increased levels for 9 of the 11 phospholipid subclasses (Supplementary Figure 4). Out of 26 phospholipid species with statistically significant ($p < 0.05$) differences between patient and control WAT, 25 were upregulated (Supplementary Table 6). When ranked according to p -value, AA-containing phospholipids LPC(20:4) ($\log_2FC = 2.05 \pm 0.38$, $p < 0.001$) and LPE(20:4) ($\log_2FC = 1.24 \pm 0.28$, $p = 0.004$) were among the top ranked lipid species (Supplementary Table 6, Figure 4d). These

results are in line with decreased PLA₂ activity in human PLAAT3-deficient WAT (Figure 4d (right panel)) (PLAAT3 human lipidomics.html).

Finally, RNA sequencing was performed on WAT samples from patient 1 and three healthy controls to identify differentially expressed genes as a consequence of *PLAAT3* deficiency. A total of 8711 genes were identified that were significantly up- or downregulated in patient WAT ($|\log_2FC| \geq 1$, raw $p < 0.05$). Of these 8711 genes, the large majority ($n=6710$) were downregulated in patient WAT, whereas 2001 genes were significantly upregulated (Figure 4e). Pathway enrichment analysis of the 100 most downregulated genes (protein coding and noncoding) identified cytoplasmic translation as the most enriched cluster, indicative of a metabolically inactive state of adipocytes. Strikingly, in human WAT, genes involved in the PPAR signaling pathway were also shown to be downregulated (Figure 4f). Transcript levels of well-established PPAR γ target genes involved in adipocyte differentiation (*PLIN1*, *FABP4*), fatty acid transport (*LPL*, *CD36*) and energy homeostasis (*LEP*, *ADIPOQ*) were significantly decreased in patient adipocytes (Figure 4e). The same analysis was performed on the top 100 most strongly upregulated genes which identified olfactory transduction and cellular dopamine response as the only significantly upregulated biological pathways. The LISA tool was used to identify TRs of gene networks within the 500 most strongly down- and upregulated genes (Figure 4g). In line with the results in mouse WAT, out of the top 10 ranked TRs of downregulated genes in human WAT, four were strongly linked to PPAR signaling including PPAR γ itself, its two main cooperating TRs CEBPA and CEBPB and its coactivator mediator complex subunit 1 (MED1).^(20, 21, 25) We used Gene Set Enrichment Analysis (GSEA) software to look for enriched gene sets among the differentially expressed genes. Among the downregulated genes, we observed an enrichment of MYC target genes and genes associated with oxidative phosphorylation and adipogenesis (Figures 4h, i). Together, these results are in line with our *Plaat3*^{-/-} mouse data and suggest a PPAR γ -mediated adipogenesis defect accompanied by reduced PLA₂ activity in human PLAAT3-deficient WAT.

***PLAAT3* knockout in adipose stem cells disrupts lipid droplet formation**

To better address the role of PLAAT3 in human adipogenesis, a custom-designed single-guide RNA (sgRNA)/Cas9 expression vector targeting the second exon of *PLAAT3* was used (Figures 5a, b) in human adipose stem cells (ASCs), isolated from abdominal subcutaneous adipose tissue⁽²⁶⁾. Human ASCs were chosen as a model because of their ability to differentiate into mature adipocytes after stimulation *in vitro* (Figure 5c). The efficiency of *PLAAT3* knockout (KO) was confirmed by Sanger sequencing of *PLAAT3* exon 2 in genomic DNA from KO ASC

cells, which revealed a high level of on-target indels with 70% insertions and 26% deletions (Figures 5a, b). Control (CTL) cells, expressing scrambled sgRNA, differentiated into adipocytes within 20 days (D20) (Figures 5c, d) and displayed strong accumulation of lipid droplets and TG content in the cytoplasm (Figures 5e, f). In contrast, *PLAAT3* KO led to a strong and significant decrease in lipid droplet formation ($p < 0.0001$) (Figures 5d, e) as well as TG content ($p < 0.0001$) (Figure 5f). The perilipin level, encoded by *PLIN1*, a mature adipocyte marker, was sharply decreased in *PLAAT3* KO cells (Figure 5g). Interestingly, the *PLAAT3* KO cells displayed decreased expression of PPAR γ (Figure 5g). We next investigated the effect of *PLAAT3* loss on insulin sensitivity. In WT and control pre-adipocytes (D0) stimulated with insulin, Western blot analysis revealed a strong increase in the phosphorylation of AKT and extracellular-regulated kinase (ERK) (Figure 5h). In contrast, the *PLAAT3* KO cells at D0 were resistant to insulin, as shown by the lack or strong decrease in the phosphorylation of these intermediates upon insulin stimulation (Figure 5h). Altogether, these findings confirm that *PLAAT3* regulates adipocyte differentiation through a cellular process involving PPAR γ .

DISCUSSION

This study establishes *PLAAT3* deficiency as a monogenic lipodystrophy syndrome associated with neurological manifestations. Our data suggest a key pathogenic role for *PLAAT3* in PPAR γ -mediated adipogenesis and thus identify *PLAAT3* as a potential therapeutic handle to regulate PPAR γ signaling, a promising therapeutic target to increase insulin sensitivity in type 2 diabetes.⁽²⁷⁾

We provide genetic evidence for the involvement of *PLAAT3* in a complex metabolic and neurological syndrome. We report seven patients from four unrelated families harboring different bi-allelic loss-of-function variants in *PLAAT3* and displaying a clinical presentation combining lipodystrophy syndrome with neurological features, consistent with the expression profile of *PLAAT3*, which is mainly expressed in adipose tissue, brain, and peripheral nerves (<https://www.gtexportal.org/home/gene/PLA2G16>). In all patients, various degrees of lipoatrophy were seen, associated with the metabolic features secondary to the loss of healthy adipose tissue. The historical classification of lipodystrophy syndrome distinguishes the generalized forms (congenital generalized lipodystrophy - CGL) with generalized fat loss apparent at birth and the partial forms (familial partial lipodystrophy - FPLD) beginning later

in life, frequently in adolescence. However, this dichotomy does not apply to all situations, and some patients with genetic lipodystrophy syndrome have already been reported with normal fat distribution at birth and the appearance of generalized fat loss later in life.^(28, 29) In patients with *PLAAT3* deficiency, both partial lipoatrophy associated with facio-cervical lipohypertrophy and generalized lipoatrophy are observed. Bi-allelic mutations in *PCYT1A* represent another example of an unclassified genetic lipodystrophy syndrome that can present as either generalized or partial fat loss.^(30, 31) All investigated *PLAAT3*-deficient patients displayed common complications associated with lipodystrophy syndrome (e.g. insulin resistance, diabetes, hypertriglyceridemia, liver steatosis, and polycystic ovary syndrome). Most patients also presented with neurological features. Demyelinating sensorimotor neuropathy was present in all investigated patients. Psychomotor retardation or intellectual disability was present in half of them.

Using multi-omics studies in human and murine WAT, we discovered a downregulated PPAR γ -mediated gene network as a downstream consequence of *PLAAT3* inactivation. PPAR γ is the master regulator of adipocyte differentiation and function and was identified as the causal gene for an autosomal dominant lipodystrophy syndrome called FPLD3.⁽³²⁾ Accordingly, our study, using CRISPR-Cas9 KO of *PLAAT3* in human ASCs, revealed an adipocyte differentiation defect characterized by a major decrease in intracellular neutral lipid levels as well as decreased expression of adipogenesis and mature adipocyte markers including PPAR γ . Insulin signaling was also altered, even in pre-adipocytes. These functional data are consistent with the lipoatrophic and insulin-resistant phenotype of *PLAAT3* patients. A similar adipocyte differentiation defect has been reported in other lipodystrophy syndrome of various genetic origins.^(29, 33-35) Our data are in line with earlier studies suggesting a central role for *PLAAT3* in adipocyte differentiation.⁽¹⁴⁻¹⁶⁾ A close link between *PLAAT3* and PPAR γ is supported by a murine adipocyte differentiation study demonstrating that *Plaat3* mRNA levels started to increase between 6 and 12h after Ppar γ -mediated initiation of differentiation.⁽¹⁴⁾ A similar observation was made for human *PLAAT3* transcripts whose expression began to rise 6h after induction of human pre-adipocyte differentiation and continued to increase during adipogenesis, like *PPAR γ* , whose expression started a few hours earlier.⁽¹⁶⁾ The expression of *PLAAT3* is therefore appropriately timed to mediate PPAR γ -driven adipogenesis. The exact mechanisms by which *PLAAT3* and PPAR γ are linked remain however partially elusive. In contrast to our results indicating a disturbed PPAR γ -mediated gene network downstream of *PLAAT3* inactivation, murine *Plaat3* was identified as a direct transcriptional target of PPAR γ ,

placing PPAR γ upstream of PLAAT3 in adipogenesis.⁽¹⁴⁾ One explanation could be that, after initial induction of PPAR γ by TFs including C/EBP β and C/EBP δ ,⁽²¹⁾ PPAR γ quickly induces PLAAT3 expression⁽¹⁴⁾, which is then needed to further sustain PPAR γ activity during and possibly after adipocyte differentiation (present study). To date, an endogenous and physiologically relevant ligand for PPAR γ has not been identified but it was shown that naturally occurring bioactive compounds including polyunsaturated fatty acids such as AA efficiently modify PPAR γ activity.^(36, 37) It is thus tempting to speculate that PLAAT3 plays a role as a PPAR γ ligand generator by liberating AA or related bioactive lipids from membrane phospholipids in WAT. Although the increased levels of AA-containing (lyso)phospholipids in murine and human PLAAT3-deficient WAT observed in the lipidomics studies would support this hypothesis, we could not detect significantly altered free AA levels or other bioactive lipid mediators in murine *Plaat3*-deficient WAT. Further research is needed to explore this possibility.

Furthermore, it cannot be excluded that PLAAT3 plays an additional PPAR γ -dependent role in mature adipocytes. Indeed, next to its central involvement in adipogenesis, PPAR γ is crucial for mature fat cell function where it regulates lipid metabolism and glucose homeostasis.⁽²⁷⁾ In line with this idea, a previous report in mice has shown chronically upregulated lipolysis in normally differentiated *Plaat3*^{-/-} adipocytes due to decreased PGE2 levels as a consequence of abrogated PLA₂ activity, which is a known inhibitor of lipolysis.^(5, 38) However, our mediator lipidomics study could not confirm the reduced PGE2 levels in murine *Plaat3*-deficient WAT and no upregulation of lipolytic enzymes on the transcript or protein level were seen. Nevertheless, we did not formally investigate lipolysis in the current study, and it is possible that it occurs in human *PLAAT3* patients. Similar observations have been made for the *LIPE* gene involved in another form of lipodystrophy syndrome.⁽³⁹⁾

Comparison of *Plaat3* null mice described in 2009 with patients carrying homozygous pathogenic *PLAAT3* variants reveals a number of similarities: a lipoatrophic phenotype, decreased circulating levels of leptin and adiponectin, insulin resistance and liver steatosis.⁽⁵⁾ Nevertheless, some differences can also be noted. Serum TG were lower in KO mice, whereas most patients display hypertriglyceridemia. Mice display smaller adipocytes (current study and previous data), whereas adipocyte size in patient WAT seems to be slightly increased.⁽⁵⁾ Such discrepancies are not unusual and, while there is no doubt on the usefulness of mouse models to study human LS, differences between human and murine fat distribution and lipid metabolism represent known limitations.^(40, 41)

Due to early rodent studies suggesting potential antiobesity and antiviral properties, modifying PLAAT3 activity was thought to be an interesting therapeutic strategy. Interestingly, while it was shown that drug targets with human genetic support are twice as likely to lead to approved drugs^(42, 43), our study suggests that blocking PLAAT3 activity too strongly could lead to unwanted metabolic side-effects secondary to a downregulation of PPAR γ -regulated gene networks.

Acknowledgements

The authors would like to thank the patients and families who participated in this study, and the GenomEast facility (IGBMC, Strasbourg, France) for exome sequencing in patient 4. We thank Machteld Baetens for in-depth CNVseq analysis. We also thank Laure Müller and Philippe Pellet for their technical help in genetic analyses in families 3 and 4. J.G. is funded by the Fondation pour la Recherche Médicale (FRM – ARF20170938613 & EQU202003010517), the Société Francophone du Diabète (SFD – R19114DD), the Mairie de Paris (Emergences – R18139DD) and the Agence Nationale de la Recherche (ANR-21-CE18-0002-01). B.D. is supported by an Odysseus type 1 Grant of the Research Foundation Flanders (G0H8318N) and a starting grant from Ghent University Special Research Fund (01N10319). N.M. is supported by the Exploratory Research for Advanced Technology (ERATO) research funding program of the Japan Science and Technology Agency (JPMJER1702) and a Grant-in-Aid for Specially Promoted Research from the Japan Society for the Promotion of Science (22H04919). The Program for Undiagnosed Diseases (UD-ProZA) is supported by the Spearhead Research Policy Program and the Fund for Innovation from the Ghent University Hospital. The Neuromendeliome Study (to C.D., Strasbourg, France) was financially supported by Agence de la Biomédecine (France). C.V. and M.A. are supported by institutional fundings from Inserm, Sorbonne Université, Assistance-Publique Hôpitaux de Paris, by the Fondation pour la Recherche Médicale (grant number EQU201903007868), and by the Association Française des Lipodystrophies (AFLIP), through a donation to Association Robert-Debré pour la Recherche Médicale (ARDRM). D.H. would like to thank Mrs. Sabine van Sprang and the whole team at the Academia Belgica, Center for History, Arts and Sciences in Rome, Italy (<https://www.academiabelgica.it>), for supporting the writing of this manuscript. The authors of this publication are members of the European Reference Network for Rare Neurological Diseases (ERN-RND) (D.H., B.D.), the Solve-RD Consortium (N.S., D.H., B.P., B.D) and the European Reference Network on Rare Endocrine Conditions (Endo-ERN, Project ID No

739527) (C.V.). For more information about the ERNs and the EU health strategy visit <http://ec.europa.eu/health/ern>. For more information about Solve-RD visit <https://solve-rd.eu>.

Author Contributions Statement

N.S., D.H., J.G., S.E.C., C.D., I.J. and B.D. wrote the manuscript. N.S., J.G., I.J. and B.D. designed the study and performed the main analyses. N.S., S.E.C., D.H., M.V., S.N., M.T., C.V., N.V.D., F.R.C., J.A.U., J.C., W.T., and S.C. were involved in phenotyping and clinical follow-up of the patients. N.S., E.B., T.R., G.D., E.D., B.F., F.A., S.K., P.H., C.D., B.P., I.J. and B.D. were involved in genotyping of the patients. S.D. and F.I. performed the proteomics analysis. J.G. designed the CRISPR-Cas9-mediated PLAAT3 knockout cellular model. M.A. provided technical support for the cell experiments. N.S. and B.D. collected adipose tissue biopsy specimens. F.O. and N.M. provided WAT from *Plaat3*^{-/-} and *Plaat3*^{+/-} mice. J.V.D. and C.V.H. performed histological analyses of human and mouse WAT. N.S., D.H., J.G., I.J. and B.D. edited the manuscript.

Competing Interests Statement

The authors declare no competing interests.

470 **Tables**

471 **Table 1. Clinical and biological characteristics of patients with biallelic truncating *PLAAT3* variants.**

	Family 1: Patient 1	Family 1: Patient 2	Family 1: Patient 3	Family 2: Patient 4	Family 3: Patient 5	Family 4: Patient 6	Family 4: Patient 7	Summary
Homozygous <i>PLAAT3</i> variant	c.16-4823_118+167del p.(Pro6ValfsTer15)	c.16-4823_118+167del p.(Pro6ValfsTer15)	c.16-4823_118+167del p.(Pro6ValfsTer15)	c.286dupG p.(Ala96GlyfsTer16)	c.339C>A p.(Cys113Ter)	c.339C>A p.(Cys113Ter)	c.339C>A p.(Cys113Ter)	
Sex	female	female	female	female	male	male	male	female (4/7), male (3/7)
Age at diagnosis (y)	38	37	25	42	2	15	11	mean: 27
Age at symptom onset (y)								
- Metabolic features	33	n.a.	18	14	4	n.a.	n.a.	
- Neurological/skeletal features	19	n.a.	8	11	1	4	4	
LS features								
Lipoatrophy	generalized	partial	partial	partial	generalized	partial	partial	partial (5/7), generalized (2/7)
Body-mass index (kg/m ²)	19.7	20.5	20.5	24.6	20.7	22.2	19.1	mean: 21
Insulin resistance	+	+	+	+	+	+	+	7/7
Liver steatosis	+	+	+	+	+	+	+	7/7
Dyslipidemia/ hypertriglyceridemia	+	+	+	+	-	+	+	6/7
Neurological features								
Psychomotor retardation/ intellectual disability	-	+	-	-	+	+	-	3/7
Demyelinating peripheral neuropathy	+	n.a.	n.a.	+	+	+	+	5/7
Musculoskeletal features								

Kyphoscoliosis	-	-	-	-	+	+	+	3/7
Chronic muscle/joint pain	+	n.a.	+	+	-	+	+	4/7
Acromegalic features	+	-	+	-	-	+	+	4/7
Additional features								
Gynecomastia	n.a.	n.a.	n.a.	n.a.	+	+	+	3/3
Dysmorphic features	prominent nose and chin	-	prominent nose and chin	-	low set ears, deep set eyes, prognathism, beaked nose, flat forehead	short neck, low hair implantation	short neck, low hair implantation	5/7

472 n.a.: not available/not applicable

FIGURE LEGENDS

Figure 1. Family pedigree structures, genetic findings and schematic display of the *PLAAT3* null variants in families 1, 2, 3 and 4.

(a) Pedigrees of families 1, 2, 3 and 4. Affected family members are shown with filled circles (females) or squares (males). Diamond-shaped symbols are used when sex is unspecified. Arrows indicate the index patients. Double horizontal lines indicate consanguinity, diagonal lines are used for deceased individuals. Genotypes, if known, are depicted in the pedigrees (-/- for homozygotes, +/- for heterozygotes). Arrows point to the index patient in the pedigree. (b) *Left panel.* Integrative Genome Viewer (IGV) screenshots showing whole exome sequencing (WES) (upper left panel) and whole genome sequencing (WGS) (lower left panel) reads mapped to the reference *PLAAT3* sequence. No reads are mapped to exon 2 of the *PLAAT3* gene in patients 1, 2 and 3, indicative of a homozygous deletion. *Right panel.* Sanger sequencing of the homozygous single nucleotide insertion in patient 4 of family 2 and the nonsense variant in patients 5, 6 and 7 in families 3 and 4. The variants are indicated with an arrow. (c) Schematic overview of the *PLAAT3* homozygous null variants identified through WES/WGS in families 1, 2, 3 and 4: the deletion of exon 2 (indicated in red) of the *PLAAT3* gene in family 1, the single base insertion in exon 3 in family 2, and the nonsense variant in exon 3 in families 3 and 4 (upper panel). The consequences of the molecular defects are also shown at the mRNA level (middle panel) and at the protein level (lower panel). The enzymatically active LRAT and a transmembrane region (TM) of PLAAT3 are depicted. All three variants result in a premature termination codon and are predicted to cause NMD.

Figure 2. Dual X-ray absorptiometry scan and clinical pictures of PLAAT3-deficient patients.

(a) Dual Energy X-ray Absorptiometry (DEXA) scan of patient 1 showing a lipoatrophic body composition with a total fat percentage of 13.8%. (b) Lateral view of patient 1 showing muscular hypertrophy in the upper and lower limbs. (c) Frontal view of patient 4 demonstrating masculine features with muscle hypertrophy and lipoatrophy of the upper and lower limbs with submental accumulation of adipose tissue. (d) Frontal view of patient 5 showing generalized lipodystrophy, gynecomastia, *genu valgum* and muscle hypertrophy of the upper limbs. (e) Lateral view of patient 5 showing gynecomastia. (f) Dorsal view of patient 5 demonstrating thoracic hyperkyphosis. (g) Foot deformities in patient 5 including *pes cavus* and hammer toes.

(h) Frontal view of patient 6 showing lipoatrophy of the trunk and gynecomastia. (i) *Acanthosis nigricans* in the axillary region of patient 6.

Figure 3. Histopathology, lipidomics, proteomics and differentially expressed gene analysis in *Plaat3*^{-/-} and *Plaat3*^{+/-} mouse WAT.

(a) Light microscopic images after staining with hematoxylin and eosin (H&E) of inguinal white adipose tissue (WAT) from a *Plaat3*^{+/-} and a *Plaat3*^{-/-} male mouse. Scale bar represents 200 μ m. (b) Box plot of adipocyte size measurement (μ m²) ($p < 0.001$) (left panel) and morphology expressed as ‘circularity’ (0-1) (right panel) of *Plaat3*^{+/-} and *Plaat3*^{-/-} mouse WAT. The center line represents the median, the box limits represent the interquartile range (IQR) and the whiskers indicate the minimum and maximum values. p -values were calculated using two-sided Independent-Samples T test. * $p < 0.05$, ** $p < 0.01$, *** $p < 0.001$. (c) Principal component analysis (PCA) of lipidomics on WAT from male ($n=6$) and female ($n=6$) *Plaat3*^{-/-} and male ($n=6$) and female ($n=6$) *Plaat3*^{+/-} mice. (d) Bar charts of phosphatidyl inositol (PI) (18:0/20:4) (male: raw $p=0.008$, female: raw $p=0.007$), phosphatidyl ethanolamine (PE) (18:0/18:2) (male: raw $p=0.003$, female: raw $p=0.004$), arachidonic acid (AA) and prostaglandin E2 (PGE2) levels depicted as the means \pm standard error of the mean (SEM). p -values were calculated using one-way analysis of variance (ANOVA), and the Benjamini-Hochberg procedure was conducted to correct for multiple testing. (e) Volcano plot showing down- (blue) and upregulated (yellow) differentially expressed genes (DEGs) with $|FC| \geq 2$ and raw $p < 0.05$ (ExactTest in edgeR) in WAT from *Plaat3*-deficient male ($n=3$) and female ($n=4$) mice compared to male ($n=4$) and female ($n=4$) *Plaat3*^{+/-} mice. DEGs above the red line: false discovery rate (FDR)-adjusted $p < 0.05$ (Benjamini-Hochberg correction). (f) Kyoto Encyclopedia of Genes and Genomes (KEGG) and Gene Ontology (GO) pathway enrichment analysis of DEGs (top 100 down- (blue) and upregulated (yellow) genes ranked according to FC with raw $p < 0.05$) using Metascape (hypergeometric test and Benjamini-Hochberg correction). (g) Top 10 transcriptional regulators (TRs) of the down- (blue) and upregulated (yellow) genes (top 100 ranked according to FC with raw $p < 0.05$) identified by LISA (one-sided Wilcoxon rank-sum test is used to assess statistical significance). (h) Volcano plot showing down- (blue) and upregulated (yellow) proteins with differential protein intensities with $|FC| \geq 1.4$ and raw $p < 0.05$ (two-sided Independent-Samples T test) in WAT from male ($n=4$) and female ($n=5$) *Plaat3*^{-/-} and male ($n=4$) compared to female ($n=5$) *Plaat3*^{+/-} mice. Proteins above the red line: FDR-adjusted $p < 0.05$ (Benjamini-Hochberg correction). (i) KEGG and GO pathway enrichment analysis of differentially abundant proteins (top 100 down- (blue)

and upregulated (yellow) ranked according to FC with raw $p < 0.05$) using Metascape. **(j)** Top 10 TRs of down- (blue) and upregulated (yellow) proteins (top 100 ranked according to FC with raw $p < 0.05$) identified using LISA.

Figure 4. Histopathology, lipidomics and differentially expressed gene analysis of patient and control WAT biopsies.

Data were obtained from upper arm subcutaneous WAT of patients 1 and 4, as well as 6 control subjects ($n=8$). **(a)** Light microscopic images after H&E, CD68 and PMP70 staining of control and patient (p1) WAT. Scale bar represents 200 μm . **(b)** Box plot of adipocyte size measurement (μm^2) ($p < 0.001$) (upper panel) and morphology expressed as ‘circularity’ (0-1) ($p = 0.003$) (lower panel) patient and control WAT. The center line represents the media, the box limits represent the interquartile range (IQR) and the whiskers indicate the minimum and maximum values. p -values were calculated using two-sided Independent-Samples T Test. $*p < 0.05$, $**p < 0.01$, $***p < 0.001$. **(c)** PCA of lipidomics in two patient samples (in purple) and six control samples (in green). **(d)** Bar charts of PI (18:0/20:4), lysophosphatidylcholine (LPC) (20:4) (raw $p < 0.001$, FDR adjusted $p = 0.017$) and lysophosphatidylethanolamine (LPE) (20:4) (raw $p = 0.004$, FDR adjusted $p = 0.044$) levels expressed as the means \pm SEM. p -values were calculated using one-way ANOVA, and the Benjamini-Hochberg procedure was conducted to correct for multiple testing. **(e)** Volcano plot showing the down- (blue) and upregulated (yellow) DEGs with $|\text{FC}| \geq 2$ and raw $p < 0.05$ (ExactTest in edgeR) in WAT from patient 1 compared to three controls ($n=4$). DEGs above the red line: FDR-adjusted $p < 0.05$ (Benjamini-Hochberg correction). **(f)** KEGG and GO pathway enrichment analysis of DEGs (top 100 down- (blue) and upregulated (yellow) genes ranked according to FC with raw $p < 0.05$) using Metascape (hypergeometric test and Benjamini-Hochberg correction). **(g)** Top 10 TRs of down- (blue) and upregulated (yellow) genes (top 500 ranked according to FC with raw $p < 0.05$) identified using LISA (one-sided Wilcoxon rank-sum test is used to assess statistical significance). **(h)** Top 10 enriched hallmark gene sets within the downregulated genes identified using Gene Set Enrichment Analysis (GSEA) software, ranked according to the normalized enrichment score (NES). **(i)** Enrichment plots with NES of the top 3 enriched hallmark gene sets.

Figure 5. PLAAT3 deficiency suppresses white adipocyte differentiation of ASCs.

Data were obtained from human adipose stem cells (ASCs), ASCs with a CRISPR-Cas9-mediated PLAAT3-knockout (KO), and ASCs transduced with a control (CTL) Cas9/scramble gRNA plasmid. p -values were determined by one-way ANOVA with the Geisser-Greenhouse

correction and Tukey's multiple comparisons test. The results are expressed as means \pm SEM, with $*p < 0.05$, $**p < 0.01$ and $***p < 0.001$, $****p < 0.0001$. **(a)** Sanger sequencing confirmed high recombination in the target region (exon 2). The expected break site is indicated by a vertical dotted line and the gRNA sequence is underlined. **(b)** The CRISPR indel pattern analysis in CTL and edited ASCs using Synthego software. The discordance plot showed a high rate of sequence misalignment after the gRNA target site, validating an editing efficiency of 96%. **(c)** A timeline representation of ASC differentiation with a hormonal cocktail. IBMX: 3-isobutyl-1-methylxanthine; D0: day 0; D10: day 10; D20: day 20. Scale bar represents 100 μ m. **(d)** Adipocyte differentiation was assessed through Oil Red-O lipid staining, with representative images shown by optical and fluorescence microscopy. Scale bar represents 100 μ m. **(e)** Quantification of Oil Red-O fluorescence normalized to DNA content (DAPI). The measurements represent three independent experiments (6 replicates each) ($p < 0.0001$). Light grey bars correspond to control conditions (ASC, CTL), dark grey bars correspond to knockout (KO) condition. **(f)** Intracellular triglyceride content at D20. The measurements represent four independent experiments. ($p < 0.0001$). Light grey bars correspond to control conditions (ASC, CTL), dark grey bars correspond to knockout (KO) condition. **(g)** Western blot analysis of adipocyte markers at D20 in ASC cells. Images are representative of three independent experiments. Quantification was performed using FIJI software and normalized to the value of CTL cells at D20. PPAR γ : KO vs ASC $p = 0.0010$, KO vs CTL $p = 0.0015$. Perilipin: KO vs ASC $p = 0.0113$, KO vs CTL $p = 0.0165$. **(h)** Activation of insulin signaling in ASCs before differentiation at D0. ASC, CTL and PLAAT3 KO cells were deprived of serum for 6 hr, stimulated with 20 nM insulin for 5 min or left untreated, and subjected to immunoblotting with antibodies against total and phospho-AKT, and extracellular-regulated kinase (ERK)1/2. Western blot images are representative of three independent experiments and were quantified using FIJI software, with normalization to CTL cells at D20 treated with insulin. pAKT: KO vs CTL $p = 0.0239$. pERK: KO vs ASC $p = 0.00471$, KO vs CTL $p = 0.0103$.

References

1. Pang XY, Cao J, Addington L, Lovell S, Battaile KP, Zhang N, et al. Structure/function relationships of adipose phospholipase A2 containing a cys-his-his catalytic triad. *J Biol Chem.* 2012;287(42):35260-74.
2. Duncan RE, Sarkadi-Nagy E, Jaworski K, Ahmadian M, Sul HS. Identification and functional characterization of adipose-specific phospholipase A2 (AdPLA). *J Biol Chem.* 2008;283(37):25428-36.
3. Uyama T, Jin XH, Tsuboi K, Tonai T, Ueda N. Characterization of the human tumor suppressors TIG3 and HRASLS2 as phospholipid-metabolizing enzymes. *Biochim Biophys Acta.* 2009;1791(12):1114-24.
4. Uyama T, Morishita J, Jin XH, Okamoto Y, Tsuboi K, Ueda N. The tumor suppressor gene H-Rev107 functions as a novel Ca²⁺-independent cytosolic phospholipase A1/2 of the thiol hydrolase type. *J Lipid Res.* 2009;50(4):685-93.
5. Jaworski K, Ahmadian M, Duncan RE, Sarkadi-Nagy E, Varady KA, Hellerstein MK, et al. AdPLA ablation increases lipolysis and prevents obesity induced by high-fat feeding or leptin deficiency. *Nat Med.* 2009;15(2):159-68.
6. Hussain I, Garg A. Lipodystrophy Syndromes. *Endocrinol Metab Clin North Am.* 2016;45(4):783-97.
7. Jéru I. Genetics of lipodystrophy syndromes. *Presse Med.* 2021;50(3):104074.
8. Brown RJ, Araujo-Vilar D, Cheung PT, Dunger D, Garg A, Jack M, et al. The Diagnosis and Management of Lipodystrophy Syndromes: A Multi-Society Practice Guideline. *J Clin Endocrinol Metab.* 2016;101(12):4500-11.
9. Letourneau LR, Greeley SAW. Congenital forms of diabetes: the beta-cell and beyond. *Curr Opin Genet Dev.* 2018;50:25-34.
10. Sollier C, Vazier C, Capel E, Lascols O, Auclair M, Janmaat S, et al. Lipodystrophic syndromes: From diagnosis to treatment. *Ann Endocrinol (Paris).* 2020;81(1):51-60.
11. Plagnol V, Curtis J, Epstein M, Mok KY, Stebbings E, Grigoriadou S, et al. A robust model for read count data in exome sequencing experiments and implications for copy number variant calling. *Bioinformatics.* 2012;28(21):2747-54.
12. Raman L, Dheedene A, De Smet M, Van Dorpe J, Menten B. WisecondorX: improved copy number detection for routine shallow whole-genome sequencing. *Nucleic Acids Res.* 2019;47(4):1605-14.
13. Sobreira N, Schiettecatte F, Valle D, Hamosh A. GeneMatcher: a matching tool for connecting investigators with an interest in the same gene. *Hum Mutat.* 2015;36(10):928-30.
14. Hummasti S, Hong C, Bensinger SJ, Tontonoz P. HRASLS3 is a PPARGgamma-selective target gene that promotes adipocyte differentiation. *J Lipid Res.* 2008;49(12):2535-44.
15. Wang Z, Chai J, Wang Y, Gu Y, Long K, Li M, et al. LncPLAAT3-AS Regulates PLAAT3-Mediated Adipocyte Differentiation and Lipogenesis in Pigs through miR-503-5p. *Genes (Basel).* 2023;14(1).
16. Michaud A, Lacroix-Pépin N, Pelletier M, Daris M, Biertho L, Fortier MA, et al. Expression of genes related to prostaglandin synthesis or signaling in human subcutaneous and omental adipose tissue: depot differences and modulation by adipogenesis. *Mediators Inflamm.* 2014;2014:451620.
17. Morishita H, Eguchi T, Tsukamoto S, Sakamaki Y, Takahashi S, Saito C, et al. Organelle degradation in the lens by PLAAT phospholipases. *Nature.* 2021;592(7855):634-8.
18. Wishart DS, Guo A, Oler E, Wang F, Anjum A, Peters H, et al. HMDB 5.0: the Human Metabolome Database for 2022. *Nucleic Acids Res.* 2022;50(D1):D622-d31.
19. Qin Q, Fan J, Zheng R, Wan C, Mei S, Wu Q, et al. Lisa: inferring transcriptional regulators through integrative modeling of public chromatin accessibility and ChIP-seq data. *Genome Biol.* 2020;21(1):32.
20. Cataldi S, Costa V, Ciccociola A, Aprile M. PPAR γ and Diabetes: Beyond the Genome and Towards Personalized Medicine. *Curr Diab Rep.* 2021;21(6):18.
21. Lefterova MI, Haakonsson AK, Lazar MA, Mandrup S. PPAR γ and the global map of adipogenesis and beyond. *Trends Endocrinol Metab.* 2014;25(6):293-302.

22. Zhang K, Chen X, Zhang P, Liu G. Perilipin2 is an Earlier Marker Than Perilipin1 for Identifying Adipocyte Regeneration in Fat Grafts. *Aesthet Surg J*. 2021;41(6):Np646-np52.
23. Olzmann JA, Carvalho P. Dynamics and functions of lipid droplets. *Nat Rev Mol Cell Biol*. 2019;20(3):137-55.
24. Kaushik S, Cuervo AM. Degradation of lipid droplet-associated proteins by chaperone-mediated autophagy facilitates lipolysis. *Nat Cell Biol*. 2015;17(6):759-70.
25. Ge K, Cho YW, Guo H, Hong TB, Guermah M, Ito M, et al. Alternative mechanisms by which mediator subunit MED1/TRAP220 regulates peroxisome proliferator-activated receptor gamma-stimulated adipogenesis and target gene expression. *Mol Cell Biol*. 2008;28(3):1081-91.
26. Gorwood J, Ejlaimesh T, Bourgeois C, Mantecon M, Rose C, Atlan M, et al. SIV Infection and the HIV Proteins Tat and Nef Induce Senescence in Adipose Tissue and Human Adipose Stem Cells, Resulting in Adipocyte Dysfunction. *Cells*. 2020;9(4).
27. Ahmadian M, Suh JM, Hah N, Liddle C, Atkins AR, Downes M, et al. PPAR γ signaling and metabolism: the good, the bad and the future. *Nat Med*. 2013;19(5):557-66.
28. Mory PB, Crispim F, Kasamatsu T, Gabbay MA, Dib SA, Moisés RS. Atypical generalized lipoatrophy and severe insulin resistance due to a heterozygous LMNA p.T10I mutation. *Arq Bras Endocrinol Metabol*. 2008;52(8):1252-6.
29. Gautheron J, Lima L, Akinci B, Zammouri J, Auclair M, Ucar SK, et al. Loss of thymidine phosphorylase activity disrupts adipocyte differentiation and induces insulin-resistant lipotrophic diabetes. *BMC Med*. 2022;20(1):95.
30. Payne F, Lim K, Girousse A, Brown RJ, Kory N, Robbins A, et al. Mutations disrupting the Kennedy phosphatidylcholine pathway in humans with congenital lipodystrophy and fatty liver disease. *Proc Natl Acad Sci U S A*. 2014;111(24):8901-6.
31. Mann JP, Savage DB. What lipodystrophies teach us about the metabolic syndrome. *J Clin Invest*. 2019;129(10):4009-21.
32. Barroso I, Gurnell M, Crowley VE, Agostini M, Schwabe JW, Soos MA, et al. Dominant negative mutations in human PPAR γ associated with severe insulin resistance, diabetes mellitus and hypertension. *Nature*. 1999;402(6764):880-3.
33. Capel E, Vatiez C, Cervera P, Stojkovic T, Disse E, Cottureau AS, et al. MFN2-associated lipomatosis: Clinical spectrum and impact on adipose tissue. *J Clin Lipidol*. 2018;12(6):1420-35.
34. Sollier C, Capel E, Aguilhon C, Smirnov V, Auclair M, Douillard C, et al. LIPE-related lipodystrophic syndrome: clinical features and disease modeling using adipose stem cells. *Eur J Endocrinol*. 2021;184(1):155-68.
35. Gautheron J, Morisseau C, Chung WK, Zammouri J, Auclair M, Baujat G, et al. EPHX1 mutations cause a lipotrophic diabetes syndrome due to impaired epoxide hydrolysis and increased cellular senescence. *Elife*. 2021;10.
36. Hernandez-Quiles M, Broekema MF, Kalkhoven E. PPAR γ in Metabolism, Immunity, and Cancer: Unified and Diverse Mechanisms of Action. *Front Endocrinol (Lausanne)*. 2021;12:624112.
37. Kim YG, Lou AC, Saghatelian A. A metabolomics strategy for detecting protein-metabolite interactions to identify natural nuclear receptor ligands. *Mol Biosyst*. 2011;7(4):1046-9.
38. Civelek E, Ozen G. The biological actions of prostanoids in adipose tissue in physiological and pathophysiological conditions. *Prostaglandins Leukot Essent Fatty Acids*. 2022;186:102508.
39. Hajnal A, Klemenz R, Schäfer R. Subtraction cloning of H-ras107, a gene specifically expressed in H-ras resistant fibroblasts. *Oncogene*. 1994;9(2):479-90.
40. Rochford JJ. Mouse models of lipodystrophy and their significance in understanding fat regulation. *Curr Top Dev Biol*. 2014;109:53-96.
41. Le Lay S, Magré J, Prieur X. Not Enough Fat: Mouse Models of Inherited Lipodystrophy. *Front Endocrinol (Lausanne)*. 2022;13:785819.
42. King EA, Davis JW, Degner JF. Are drug targets with genetic support twice as likely to be approved? Revised estimates of the impact of genetic support for drug mechanisms on the probability of drug approval. *PLoS Genet*. 2019;15(12):e1008489.

43. Nelson MR, Tipney H, Painter JL, Shen J, Nicoletti P, Shen Y, et al. The support of human genetic evidence for approved drug indications. *Nat Genet.* 2015;47(8):856-60.

METHODS

This research complies with all relevant ethical regulation and was approved by the Ethics Committee of the University Hospital of Ghent (EC: 2019/1430). Data collection and analysis were not performed blind to the conditions of the experiment. No animals or data points have been excluded from the analyses.

Patient clinical characteristics

All seven patients were clinically evaluated by an endocrinologist and a neurologist. Blood samples were taken to determine the levels of fasting glucose, HbA1c, insulin, cholesterol, triglycerides and leptin. Plasma insulin measurements were performed using the Roche ECLIA technology, and leptin was measured through a radioimmunoassay. Lipoatrophy and regional fat accumulation were objectified using MRI or CT scan imaging. In two patients, dual X-ray absorptiometry was performed to evaluate body composition. In five patients, EMG was performed, and in four patients, brain MRI was performed. In one patient and one control, biopsy specimens of upper arm subcutaneous WAT were obtained for histopathological examination with hematoxylin and eosin and anti-CD68 staining after informed consent of the patient and its caregiver. Quantification of the results was performed using ImageJ software.⁹ Statistical analysis was done in SPSS Statistics 27. Written informed consent for multiomics analysis and publication of clinical pictures was obtained from all patients and control individuals. For multi-omics analysis we obtained upper arm subcutaneous WAT biopsies of patients 1 and 4, as well as six healthy, lean, female controls with ages between 25 and 60 years old. The samples size was restricted due to the limited availability of WAT biopsies. No power analysis was performed.

Genomics

Genetic studies in family 1 were initiated by the UD-ProZA team at Ghent University Hospital and included SNP-array-based homozygosity mapping, Sanger sequencing and cDNA analysis

of *BSCL2*, whole exome sequencing (WES), low-pass shallow whole genome sequencing (CNV-sequencing) and whole genome sequencing (WGS).

Homozygosity mapping: Genotyping for homozygosity mapping was performed in three affected and two unaffected members of family 1 using 200K genome-wide HumanCytoSNP-12 v2 BeadChip single nucleotide polymorphism (SNP) arrays (Illumina, San Diego, CA). The position of the probes was based on NCBI build GRCh37. Homozygous regions shared between affected members were detected using the PLINK algorithm (v1.07, default settings).⁽⁴⁴⁾

BSCL2 mutation screening: Sequencing of *BSCL2* was performed using Sanger sequencing after PCR amplification of all exons including splice junctions. Extracted mRNA from cultured lymphocytes was reverse transcribed to cDNA. The region covering *BSCL2* exons 2 to 9 was amplified by PCR from this cDNA. The PCR product was migrated on an agarose gel and its size was compared to that obtained from a control subject.

Whole-exome sequencing (WES): WES was performed on the Illumina NovaSeq 6000 Platform after enrichment of gDNA with SureSelectXT Low Input Human All Exon v7 (Agilent Technologies). The BWA-MEM 0.7.17 algorithm was used for read mapping against the human genome reference sequence (NCBI, GRCh37.p5/hg19), duplicate read removal, and variant calling. Variant calling and filtering were performed using Seqplorer, an in-house developed tool for the analysis of WES data. The position of the called variants is based on NCBI build GRCh38. A minimum of 90% of the interrogated genes had a coverage of >20x. Variant classification was performed according to the ACMG guidelines⁽⁴⁵⁾ CNVs were detected with ExomeDepth.⁽¹¹⁾

Molecular karyotyping was performed by means of low-pass whole-genome sequencing (CNV-seq) on an Illumina NovaSeq 6000 with a genome wide resolution of 100 kb (GRCh38).

Whole-genome sequencing was performed by Macrogen on an Illumina NovaSeq 6000 platform. Fastq-files were aligned against the hg38 reference genome with BWA-MEM (v0.7.17). Files were converted to BAM format, duplicate marked, and sorted and indexed using Samtools (v1.9)⁽⁴⁶⁾ and Picard (v2.21.6). Structural variants (SVs) were then called using three different callers, namely DELLY (v0.8.3)⁽⁴⁷⁾, LUMPY (v0.2.13)⁽⁴⁸⁾ and Manta (v1.6.0)⁽⁴⁹⁾. Standard settings were used for all.

In family 2, genetic analysis was initiated by a clinical geneticist at Hôpital de Haute-pierre in Strasbourg and included the analysis of neuropathy and lipodystrophy gene panels, WES and Sanger sequencing. Genetic studies in families 3 and 4 were initiated at Hôpital Pitié-Salpêtrière in Paris and consisted of the analysis of a gene panel including genes involved in lipodystrophic syndromes and WES followed by Sanger sequencing of the region encompassing the *PLAAT3* variant. WES was performed for the index case as part of the ‘Neuromendeliome’ study, including 26 patients with unsolved syndromes affecting the nervous system. Paired-end sequencing libraries were prepared using the Agilent SureSelect XT Human All Exon v7 Enrichment kit. Sequencing (2x100 bases) was performed on a HiSeq2500 (Illumina) on the GenomEast platform (IGBMC, Illkirch, France). Image analysis and base calling were performed using CASAVA v1.8.2 (Illumina). Reads were mapped onto the reference genome Hg19 using BWA v0.7.5a.⁽⁵⁰⁾ Elimination of duplicate reads and base quality recalibration were performed using Picard v1.122. Realignment around indels was performed with GATK v3.2-2. Reads mapping to several positions in the genome were excluded using Samtools v0.1.19.⁽⁴⁶⁾ Variant calling was done using GATK v3.2-2 Unified genotyper.⁽⁵¹⁾ Variants were annotated using GATK v3.2-2⁽⁵¹⁾, SnpE_ v2.0.5⁽⁵²⁾ and SnpSift v4.4l⁽⁵³⁾.

Generation of *Plaat3*^{-/-} mice

All mouse (C57BL/6J) experiments were approved by the Institutional Animal Care and Use Committee of the University of Tokyo (Medical-P17-084) and the Animal Care and Use Committee of the National Institute of Quantum and Radiological Science and Technology (1610111 and 1610121). *Plaat3*^{+/-} mice (C57BL/6J) were intercrossed to obtain *Plaat3*^{-/-} mice.⁽¹⁷⁾ Genotyping of *Plaat3*^{+/-} and *Plaat3*^{-/-} mice was performed by PCR using primers flanking the target site (forward primer, 5'-GAAAGAACTGCTGTGCCATGTGGCC-3'; reverse primer, 5'-ACCTGATCACTCCGAGGAACTCCATAGC-3') and subsequent acrylamide gel electrophoresis. Wild-type and mutated alleles were detected as 207-bp and 191-bp bands, respectively. 24 inguinal WAT specimens were obtained from 6 male *Plaat3*^{-/-}, 6 male *Plaat3*^{+/-}, 6 female *Plaat3*^{-/-}, and 6 female *Plaat3*^{+/-} at the age of 11 weeks. All mice were housed in a specific pathogen-free room maintained at a constant ambient temperature of 20-22°C, 40-60% of humidity under a 12-hour light/dark cycle with free access to water and food. Mice were fed sterilized (30kGy) CLEA Rodent Diet CE-2 standard pellet chow (CLEA Japan, Inc., Tokyo, Japan). No statistical methods were used to pre-determine samples sizes but our

sample sizes are similar to those reported in previous publications.^(5, 17) Data collection and analysis were not performed blind to the conditions of the experiments.

RNA sequencing

RNA sequencing was performed on 15 inguinal mouse WAT samples. Seven *Plaat3*^{-/-} specimens (3 males, 4 females) were compared to 8 *Plaat3*^{+/-} littermates (4 males, 4 females). Additionally, RNA sequencing was performed on an upper arm WAT sample of patient 1 and three healthy lean controls (females, between 30 and 58 years of age and of European Caucasian descent, BMI ranging between 19 and 22 kg/m²).

RNA paired-end sequencing was performed by MacroGen on an Illumina platform. Library preparation was performed using the SMARTer Universal Low Input RNA Kit (Takara Bio Inc, #634936) and the TruSeq RNA Sample Prep Kit v2 (Illumina, Inc., #RS-122-2101). Trimmed reads were mapped to the reference genome with HISAT2.⁽⁵⁴⁾ After read mapping, Stringtie was used for transcript assembly.⁽⁵⁵⁾ The expression profile was calculated for each sample and transcript/gene as read count, FPKM (Fragment per Kilobase of transcript per Million mapped reads) and TPM (Transcripts per Kilobase Million). Differentially Expressed Genes (DEG) analysis was performed on a comparison pair (test vs control) using edgeR.⁽⁵⁶⁾ Functional enrichment analysis of KEGG and GO pathways⁽⁵⁷⁾ within 100 most strongly down- and upregulated genes was performed using the Metascape tool.⁽⁵⁸⁾ To identify potential transcriptional regulators (TRs) of the top 100 (mouse WAT) or 500 (human WAT) down- and upregulated genes we performed LISA (epigenetic landscape in silico deletion analysis; <http://lisa.cistrome.org/>), which is designed to combine a comprehensive database of human and mouse DNase-seq, H3K27ac ChIP-seq, and TR ChIP-seq to identify TRs that regulate a query gene set.⁽¹⁹⁾

Lipidomics and histopathology

Lipidomics analysis was performed on inguinal WAT of 12 *Plaat3*^{-/-} (6 male, 6 female) and 12 *Plaat3*^{+/-} (6 male, 6 female) mice and subcutaneous upper inner arm WAT specimens from two patients (patients 1 and 4) and 6 control individuals (all female, between 27 and 58 years of age and of European Caucasian descent, BMI ranging between 19 and 22 kg/m²) in collaboration with LipometrixTM, the lipidomics core at KU Leuven in Belgium. The subcutaneous adipose

tissue specimens were obtained through an open biopsy, and the site of sampling was identical for all patients and controls. After lipid extraction and sample normalization, hydrophilic interaction liquid chromatography-mass spectrometry (HILIC LC-MS/MS) was performed, enabling quantification of 1800 lipid species across 18 different lipid classes (<https://www.lipometrix.be>)

Part of the mouse inguinal WAT biopsies were thawed and fixed in 10% neutral-buffered formalin for ~27 hours, paraffin-embedded and stained with hematoxylin and eosin. Light microscopic images were analyzed using ImageJ software.⁹

Lipid extraction

A sample containing 10 µg of protein was mixed with 800 µl 1 N HCl:CH₃OH 1:8 (v/v), 900 µl CHCl₃, 200 µg/ml of the antioxidant 2,6-di-tert-butyl-4-methylphenol (BHT; Sigma Aldrich) and 3 µl of SPLASH® LIPIDOMIX® Mass Spec Standard (#330707, Avanti Polar Lipids). After vortexing and centrifugation, the lower organic fraction was collected and evaporated using a Savant Speedvac spd111v (Thermo Fisher Scientific) at room temperature and the remaining lipid pellet was stored at - 20°C under argon.

Mass spectrometry

Just before mass spectrometry analysis, lipid pellets were reconstituted in 100% ethanol. Lipid species were analyzed by liquid chromatography electrospray ionization tandem mass spectrometry (LC-ESI/MS/MS) on a Nexera X2 UHPLC system (Shimadzu) coupled with a hybrid triple quadrupole/linear ion trap mass spectrometer (6500+ QTRAP system; AB SCIEX). Chromatographic separation was performed on an XBridge amide column (150 mm × 4.6 mm, 3.5 µm; Waters) maintained at 35°C using mobile phase A [1 mM ammonium acetate in water-acetonitrile 5:95 (v/v)] and mobile phase B [1 mM ammonium acetate in water-acetonitrile 50:50 (v/v)] in the following gradient: (0-6 min: 0% B → 6% B; 6-10 min: 6% B → 25% B; 10-11 min: 25% B → 98% B; 11-13 min: 98% B → 100% B; 13-19 min: 100% B; 19-24 min: 0% B) at a flow rate of 0.7 mL/min which was increased to 1.5 mL/min from 13 minutes onwards. SM, CE, CER, DCER, HCER and LCER were measured in positive ion mode with precursor scans of 184.1, 369.4, 264.4, 266.4, 264.4 and 264.4 respectively. TAG, DAG and MAG were measured in positive ion mode with a neutral loss scan for one of the fatty acyl moieties. PC, LPC, PE, LPE, PG, PI and PS were measured in negative ion mode by fatty acyl fragment ions. Lipid quantification was performed by scheduled multiple reaction monitoring (MRM), and the transitions were based on neutral losses or typical product ions as described

above. The instrument parameters were as follows: curtain gas = 35 psi; collision gas = 8 a.u. (medium); ion spray voltage = 5500 V and -4,500 V; temperature = 550°C; ion source gas 1 = 50 psi; ion source gas 2 = 60 psi; declustering potential = 60 V and -80 V; entry potential = 10 V and -10 V; collision cell exit potential = 15 V and -15 V.

The following fatty acyl moieties were taken into account for the lipidomic analysis: 14:0, 14:1, 16:0, 16:1, 16:2, 18:0, 18:1, 18:2, 18:3, 20:0, 20:1, 20:2, 20:3, 20:4, 20:5, 22:0, 22:1, 22:2, 22:4, 22:5 and 22:6, except for TGs, which considered 16:0, 16:1, 18:0, 18:1, 18:2, 18:3, 20:3, 20:4, 20:5, 22:2, 22:3, 22:4, 22:5, and 22:6.

Data Analysis

Peak integration was performed with the MultiQuantTM software version 3.0.3. Lipid species signals were corrected for isotopic contributions (calculated with Python Molmass 2019.1.1) and were quantified based on internal standard signals and adheres to the guidelines of the Lipidomics Standards Initiative (LSI) (level 2 type quantification as defined by the LSI). Unpaired T-test p-values and FDR corrected p-values (using the Benjamini/Hochberg procedure) were calculated in Python StatsModels version 0.10.1.

Proteomics

Sample preparation

Proteomics analysis was performed on inguinal WAT of 9 *Plaat3*^{-/-} (4 male, 5 female) and 9 *Plaat3*^{+/-} (4 male, 5 female) mice. Inguinal WAT tissue in 1.5 ml tubes was mechanically disrupted by 2 cycles of grinding with a disposable micropestle and freeze-thawing. Then, 250 µl lysis buffer containing 5% sodium dodecyl sulfate (SDS) and 50 mM triethylammonium bicarbonate (TEAB), pH 8.5, was added to the tissue, and the samples were ground once more with a micropestle to disrupt any remaining intact material. The tubes were spun down shortly, each sample was divided over 3 wells of a PIXULTM 96-well plate (Active Motif) and samples were sonicated with a PIXULTM Multisample sonicator (Active Motif) for 30 minutes with default settings (Pulse 50 cycles, PRF 1 kHz, Burst Rate 20 Hz). After centrifugation for 5 min at 2204 x g at room temperature (RT), the bottom (non-lipid) layer was transferred to new tubes and the protein concentration was measured by bicinchoninic acid (BCA) assay (Thermo Scientific). From each sample, 100 µg of protein was isolated to continue the protocol. Proteins were reduced by the addition of 15 mM dithiothreitol and incubation for 30 minutes at 55°C

and then alkylated by the addition of 30 mM iodoacetamide and incubation for 15 minutes at RT in the dark. Phosphoric acid was added to a final concentration of 1.2%, and subsequently, samples were diluted 7-fold with binding buffer containing 90% methanol in 100 mM TEAB, pH 7.55. The samples were loaded on a 96-well S-TrapTM plate (Protifi), placed on top of a deepwell plate, and centrifuged for 2 min at 1,500 x g at RT. After protein binding, the S-trapTM plate was washed three times by adding 200 μ l binding buffer and centrifugation for 2 min at 1,500 x g at RT. A new deepwell receiver plate was placed below the 96-well S-TrapTM plate and 50 mM TEAB containing trypsin (1/100, w/w) was added for digestion overnight at 37°C. Using centrifugation for 2 min at 1,500 x g, peptides were eluted three times, first with 80 μ l 50 mM TEAB, then with 80 μ l 0.2% formic acid (FA) in water and finally with 80 μ l 0.2% FA in water/acetonitrile (ACN) (50/50, v/v). Eluted peptides were dried completely by vacuum centrifugation.

TMTproTM 18-plex labels (0.5 mg, Thermo Fisher Scientific) were equilibrated to RT immediately before use and dissolved in 20 μ l anhydrous acetonitrile (ACN). The dried peptides were resuspended in 80 μ l 100 mM TEAB (pH 8.5), the peptide concentration was determined on a Lunatic spectrophotometer (Unchained Labs)⁽⁵⁹⁾ and the peptide amount was adjusted to 40 μ g for each sample. Peptides were labeled for 1 hour at RT using 0.5 mg of TMTProTM label (labels used: 135N, 132C, 131N, 132N, 134N, 133C, 133N, 134C, 131C: *Plaat3*^{+/-} heterozygous replicates; 130C, 128N, 126C, 127C, 129C, 129N, 128C, 130N, 127N: *Plaat3*^{-/-} homozygous replicates). The reaction was quenched for 15 min at RT by the addition of 4.2 μ l of 5% hydroxylamine. The 18 labeled samples were combined, and 100 μ g labeled peptides were isolated, dried by vacuum centrifugation, redissolved in 100 μ l 0.1% TFA and desalted on a reversed phase (RP) C18 OMIX tip (Agilent). The tip was first washed 3 times with 100 μ l pre-wash buffer (0.1% TFA in water/ ACN (20:80, v/v)) and pre-equilibrated 5 times with 100 μ l of wash buffer (0.1% TFA in water) before the sample was loaded on the tip. After peptide binding, the tip was washed 3 times with 100 μ l of wash buffer, and peptides were eluted twice with 100 μ l elution buffer (0.1% TFA in water/ACN (40:60, v/v)). The combined elutions were dried in a vacuum concentrator.

Vacuum-dried peptides were redissolved in 100 μ l loading solvent A (0.1% TFA in water/ACN (98:2, v/v)), and 95 μ l was injected for fractionation by RP-HPLC (Agilent series 1200) connected to a Probot fractionator (LC Packings). Peptides were first loaded in solvent A on a 4 cm precolumn (made in-house, 250 μ m internal diameter (ID), 5 μ m C18 beads, Dr. Maisch) for 10 min at 25 μ l/min and then separated on a 15 cm analytical column (made in-house, 250

μm ID, 3 μm C18 beads, Dr Maisch). Elution was performed using a linear gradient from 100% RP-HPLC solvent A (10 mM ammonium acetate (pH 5.5) in water/ACN (98:2, v/v)) to 100% RP-HPLC solvent B (70% ACN, 10 mM ammonium acetate (pH 5.5)) in 100 min at a constant flow rate of 3 μL/min. Fractions were collected every minute between 20 and 92 minutes and pooled every 24 minutes to generate a total of 24 samples for LC-MS/MS analysis. All 24 fractions were dried under vacuum in HPLC inserts and stored at -20°C until further use.

LC-MS/MS analysis

Each fraction was solubilized in 20 μL loading solvent A (0.1% TFA in water:ACN (98:2, v:v)) moments before analysis. 15 μl of the sample measured on Dropsense16 (Unchained Labs) was injected for LC-MS/MS analysis with an Ultimate 3000 RSLCnano system in-line connected to an Orbitrap Fusion Lumos mass spectrometer (Thermo). Trapping was performed at 20 μl/min for 2 min in loading solvent A on a 20 mm trapping column (Thermo Scientific, 300 μm internal diameter (I.D.), 5 μm beads). The peptides were separated on a 110 cm prototype μPAC™ column (Thermo Scientific). It was kept at a constant temperature of 50°C. Peptides were eluted by a linear gradient reaching 26.4% MS solvent B (0.1% FA in water/acetonitrile (2:8, v/v)) after 45 min, 44% MS solvent B at 55 min, 56% MS solvent B at 60 min, followed by a 10-min wash at 56% MS solvent B and re-equilibration with MS solvent A (0.1% FA in water). In the first 15 min, the flow rate was set to 600 nl/min after which it was kept constant at 300 nl/min.

The mass spectrometer was operated in data-dependent mode. Full-scan MS spectra (375-1500 m/z) were acquired at a resolution of 120,000 in the Orbitrap analyzer after accumulation to a target AGC value of 400,000 with a maximum injection time of 50 ms. The precursor ions were filtered for charge states (2-7 required), dynamic exclusion (60 s; +/- 10 ppm window) and intensity (minimal intensity of 5E4). The precursor ions were selected in the quadrupole with an isolation window of 0.7 Da and accumulated to an AGC target of 1E4 or a maximum injection time of 50 ms and activated using CID fragmentation (35% NCE). The fragments were analyzed in the Ion Trap Analyzer at the turbo scan rate. The 10 most intense MS2 fragments were selected in the ion trap using MS3 multi-notch isolation windows of 2 m/z. An orbitrap resolution of 60k was used with an AGC target of 1.0e5 or a maximum injection time of 118 ms and activated using HCD fragmentation (65% NCE). QCloud was used to control instrument longitudinal performance during the project.⁽⁶⁰⁾

Data analysis

LC-MS/MS runs of all 18 samples were searched together using the MaxQuant algorithm (version 2.1.3.0) with mainly default search settings, including a false discovery rate set at 1% at the peptide and protein levels. Spectra were searched against the mouse protein sequences in the Swiss-Prot database (database release version of January 2022), containing 21,986 sequences (www.uniprot.org). The mass tolerance for precursor and fragment ions was set to 4.5 and 20 ppm, respectively, during the main search. Enzyme specificity was set to the C-terminus of arginine and lysine, also allowing cleavage at Arg/Lys-Pro bonds with a maximum of two missed cleavages. Variable modifications were set to oxidation of methionine residues and acetylation of protein N-termini whereas carbamidomethylation of cysteine residues was set as a fixed modification. Only proteins with at least one unique or razor peptide were retained, leading to the identification of 4,036 proteins. MS3-based quantification using TMTpro labels was chosen as the quantification method, and a minimum ratio count of 2 unique peptides was required for quantification. Further data analysis of the shotgun results was performed with an in-house R script using the proteinGroups output table from MaxQuant. Reverse database hits were removed, reporter intensities were log2 transformed, and median-normalized and replicate samples were grouped. Proteins with less than three valid values in at least one group were removed and missing values were imputed from a normal distribution centered around the detection limit (DEP package), leading to a list of 4,033 quantified proteins in the experiment, used for further data analysis.⁽⁶¹⁾ To compare protein abundance between pairs of sample groups, statistical testing for differences between two group means was performed using the limma package.⁽⁶²⁾ Statistical significance for differential regulation was set by a raw $p < 0.05$ and fold change $|\log_2 \text{FC}| \geq 0.5$. The mass spectrometry proteomics data have been deposited to the ProteomeXchange Consortium via the PRIDE partner repository with the dataset identifier PXD038815.

CRISPR/Cas9-mediated deletion of *PLAAT3*

The lentiviral plasmid plentiCRISPRv2 was a gift from the Zhang lab (Addgene, MA, USA; plasmid #52961) and contains hSpCas9, a guide RNA (gRNA), and a puromycin resistance sequence. The gRNA targeting exon 2 of *PLAAT3* was designed and checked for efficiency (<http://cistrome.org/SSC>) and specificity (<http://crispr.mit.edu>). The web-based tool CRISPOR (<http://crispor.tefor.net>) was used to evaluate potential off-target sequences. Subsequently, the gRNA was cloned into plentiCRISPRv2, and lentiviruses were produced by the VVTG platform

(SFR Necker, France). ASCs were infected with viral particles at a minimal titer of 10^8 transducing units per mL. Forty-eight hours postinfection, the cells were selected with $5 \mu\text{g/mL}$ puromycin dihydrochloride (#P9620; Sigma-Aldrich). Surviving cells were propagated and the heterogeneous cell pool was used for experiments. The percentage of on-target recombination including insertions and deletions (indels) in the genomic DNA from the KO cells was evaluated by Sanger sequencing followed by analysis using the Synthego web-based tool (<https://ice.synthego.com>). The gRNA sequence used in this study is provided in Supplementary Table 7.

Cell culture

Human ASCs were isolated from surgical samples of subcutaneous abdominal adipose tissue from a control woman with normal BMI. Adipose tissue samples were enzymatically digested with collagenase B (0.2%). After centrifugation, the stromal vascular fraction was filtered, rinsed, plated and cultured in α -MEM with 10% FCS, 2 mmol/L glutamine, 1% P/S (10,000 UI/mL), 1% Hepes and Fibroblast Growth Factor-2 (145 nmol/L). After 24 h, only ASCs adhered to plastic surfaces, while other cells were removed after culture medium replacement. ASCs were maintained in an undifferentiated state in high-glucose (4.5 g/L) DMEM supplemented with 10% newborn calf serum and 1% P/S. All culture conditions were kept constant throughout the experiments. ASC differentiation was induced as described previously.^(29, 35) Briefly, 2-day postconfluent cultures were treated with high-glucose (25 mmol/L) DMEM supplemented with 10% FCS, 1% P/S, 1 $\mu\text{mol/L}$ dexamethasone, 1 $\mu\text{mol/L}$ rosiglitazone, 250 $\mu\text{mol/L}$ IBMX and 0.17 $\mu\text{mol/L}$ insulin for ten days. The medium was then replaced with high-glucose DMEM supplemented with 10% FCS, 1% P/S, 1 $\mu\text{mol/L}$ rosiglitazone and 0.17 $\mu\text{mol/L}$ insulin and changed to fresh medium every 2 days until the 20th day.

Oil Red-O staining, image processing, and quantification

Intracellular lipids were stained with Oil Red-O (#O0625; Sigma-Aldrich). Cells were washed with PBS and fixed with 4% PFA in PBS for 10 min. Fixed cells were incubated with Oil Red-O solution for 1 h at room temperature and then with DAPI (#D1306, Thermo Fischer Scientific) for 5 min. Fluorescence images were generated with an IX83 Olympus microscope, acquired with Cell-Sens V1.6 and analyzed with FIJI software. Images of 8-10 different areas per condition were visualized by fluorescence microscopy using mCherry and DAPI filters, followed by computer image analysis using FIJI software. Briefly, analysis was performed by

threshold converting the 8-bit red-green-blue image into a binary image, which consists only of pixels representing lipid droplets (*i.e.*, red). Importantly, after separation, the binary image was manually compared with the original image for consistency and correct binary conversion. The area occupied by lipid droplets in the image was displayed by FIJI software as surface area in μm^2 and normalized to cell number by semiautomated counting of DAPI-stained nuclei.

Quantification of intracellular triglyceride content

Intracellular lipids were extracted from differentiated ASC using hexane/isopropyl alcohol (3:2). Cells were washed and incubated with hexane/isopropyl alcohol (3:2, vol/vol) using 500 μL per well in 6-well culture plates on a shaker (80 rpm/minute) at room temperature for 60 minutes. The content of each well was then transferred into a glass tube for nitrogen evaporation of the organic solvent. After evaporation, the lipids were resuspended in isopropyl alcohol and transferred into duplicate 96-well plates for analysis after drying. Triglycerides were measured using the Infinity™ Triglyceride kit (Thermo Fischer Scientific) according to manufacturer's instructions. The absorbance of each well was measured using a Tecan microplate reader (TECAN, Männedorf, Switzerland) and converted to concentration based on a standard curve. The results were normalized to the cell protein content.

Western blot

Cells were homogenized in NP-40 lysis buffer to obtain protein lysates. Thirty micrograms of protein extracts were separated by sodium dodecyl sulfate polyacrylamide gel electrophoresis (SDS-PAGE), transferred to a polyvinylidene difluoride membrane and analyzed by immunoblotting. Adipose tissues were dissociated and homogenized with ceramic beads and NP-40 lysis buffer using a Bead Ruptor (#19-042E, OMNI International, GA, USA). Western blot quantification was performed in triplicate using Fiji software (Open source), and the results were normalized to the tubulin, ERK or AKT protein levels.

Data availability

All relevant data generated and analyzed in this study are included in the article. Mouse RNA-seq data have been deposited in the Gene Expression Omnibus (GEO) at NCBI (GSE233433). The mouse mass spectrometry proteomics data have been deposited to the ProteomeXchange Consortium via the PRIDE partner repository with the dataset identifier PXD038815. The human and mouse lipidomics data are available as supplementary files (Plaat3 mouse

lipidomics.html; Plaatz mouse mediator lipidomics.html; PLAAT3 human lipidomics.html).

For reasons of privacy, clinical patient sequencing data are not publicly available..

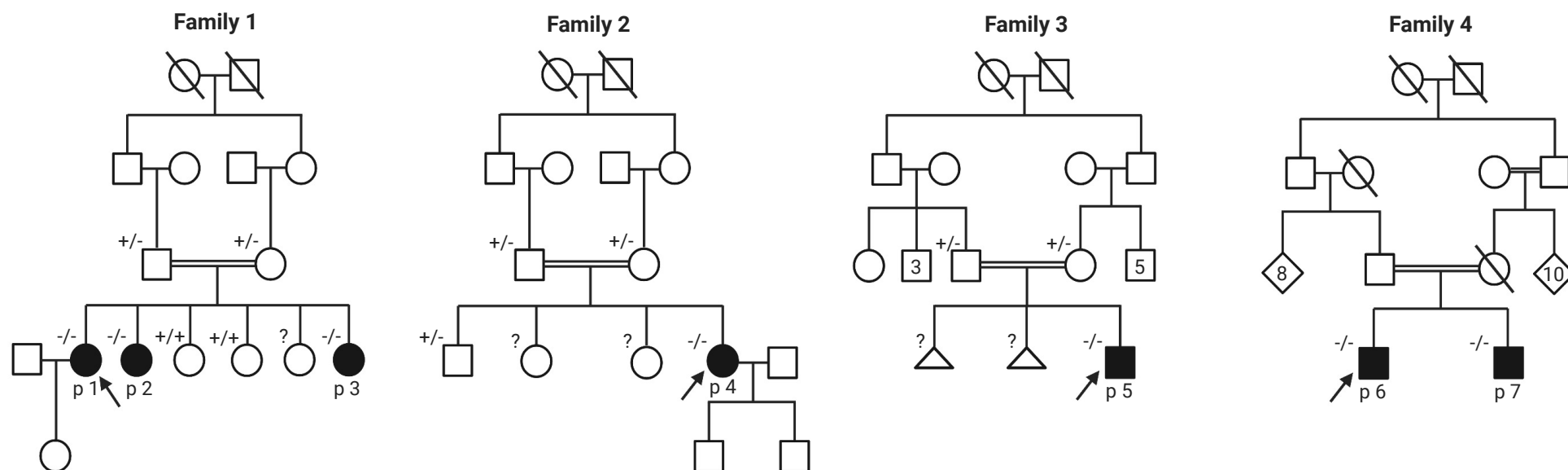
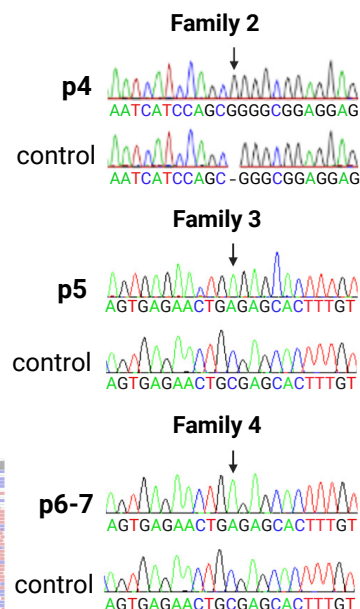
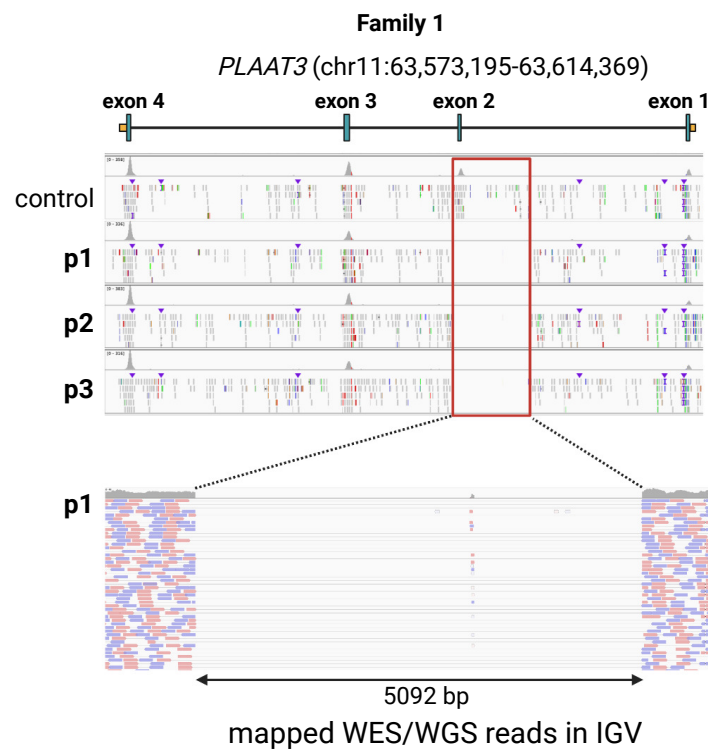
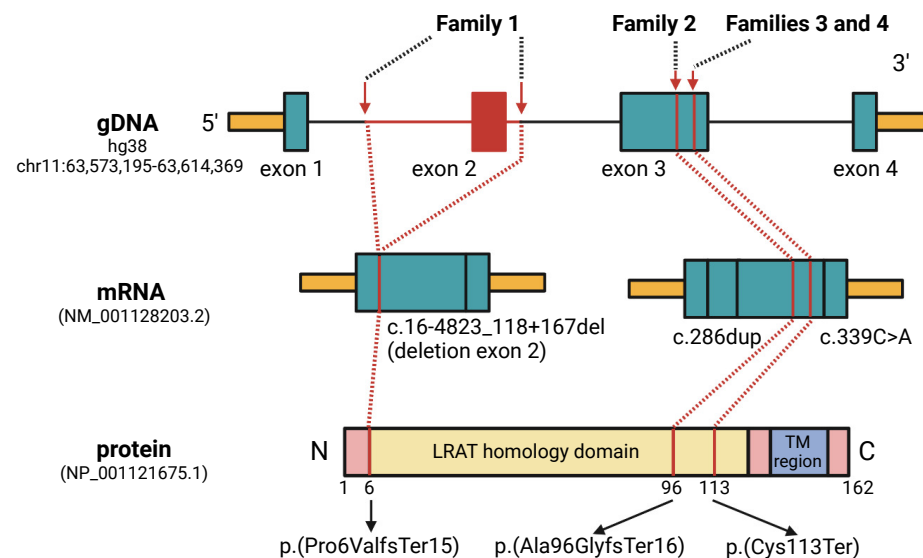
Code availability

All multi-omics related software used in this study is published and cited either in the main text or Methods. No custom code was used for data processing or analysis of the transcriptomics, proteomics or lipidomics datasets. Data analysis approaches using published software packages are described in the Methods and Supplementary Notes. For patients' privacy reasons the Seqplorer codes for variant calling and filtering won't be publicly available.

Methods-only references

44. Slifer SH. PLINK: Key Functions for Data Analysis. *Curr Protoc Hum Genet*. 2018;97(1):e59 <https://doi.org/10.1002/cphg.59>.
45. Richards S, Aziz N, Bale S, Bick D, Das S, Gastier-Foster J, et al. Standards and guidelines for the interpretation of sequence variants: a joint consensus recommendation of the American College of Medical Genetics and Genomics and the Association for Molecular Pathology. *Genet Med*. 2015;17(5):405-24 <https://doi.org/10.1038/gim.2015.30>.
46. Li H, Handsaker B, Wysoker A, Fennell T, Ruan J, Homer N, et al. The Sequence Alignment/Map format and SAMtools. *Bioinformatics*. 2009;25(16):2078-9 <https://doi.org/10.1093/bioinformatics/btp352>.
47. Rausch T, Zichner T, Schlattl A, Stütz AM, Benes V, Korbel JO. DELLY: structural variant discovery by integrated paired-end and split-read analysis. *Bioinformatics*. 2012;28(18):i333-i9 <https://doi.org/10.1093/bioinformatics/bts378>.
48. Layer RM, Chiang C, Quinlan AR, Hall IM. LUMPY: a probabilistic framework for structural variant discovery. *Genome Biol*. 2014;15(6):R84 <https://doi.org/10.1186/gb-2014-15-6-r84>.
49. Chen X, Schulz-Trieglaff O, Shaw R, Barnes B, Schlesinger F, Källberg M, et al. Manta: rapid detection of structural variants and indels for germline and cancer sequencing applications. *Bioinformatics*. 2016;32(8):1220-2 <https://doi.org/10.1093/bioinformatics/btv710>.
50. Li H, Durbin R. Fast and accurate short read alignment with Burrows-Wheeler transform. *Bioinformatics*. 2009;25(14):1754-60 <https://doi.org/10.1093/bioinformatics/btp324>.
51. DePristo MA, Banks E, Poplin R, Garimella KV, Maguire JR, Hartl C, et al. A framework for variation discovery and genotyping using next-generation DNA sequencing data. *Nat Genet*. 2011;43(5):491-8 <https://doi.org/10.1038/ng.806>.
52. Cingolani P, Platts A, Wang le L, Coon M, Nguyen T, Wang L, et al. A program for annotating and predicting the effects of single nucleotide polymorphisms, SnpEff: SNPs in the genome of *Drosophila melanogaster* strain w1118; iso-2; iso-3. *Fly (Austin)*. 2012;6(2):80-92 <https://doi.org/10.4161/fly.19695>.
53. Cingolani P, Patel VM, Coon M, Nguyen T, Land SJ, Ruden DM, et al. Using *Drosophila melanogaster* as a Model for Genotoxic Chemical Mutational Studies with a New Program, SnpSift. *Front Genet*. 2012;3:35 <https://doi.org/10.3389/fgene.2012.00035>.

54. Kim D, Paggi JM, Park C, Bennett C, Salzberg SL. Graph-based genome alignment and genotyping with HISAT2 and HISAT-genotype. *Nat Biotechnol.* 2019;37(8):907-15 <https://doi.org/10.1038/s41587-019-0201-4>.
55. Pertea M, Pertea GM, Antonescu CM, Chang TC, Mendell JT, Salzberg SL. StringTie enables improved reconstruction of a transcriptome from RNA-seq reads. *Nat Biotechnol.* 2015;33(3):290-5 <https://doi.org/10.1038/nbt.3122>.
56. Robinson MD, McCarthy DJ, Smyth GK. edgeR: a Bioconductor package for differential expression analysis of digital gene expression data. *Bioinformatics.* 2010;26(1):139-40 <https://doi.org/10.1093/bioinformatics/btp616>.
57. Kanehisa M, Goto S, Sato Y, Furumichi M, Tanabe M. KEGG for integration and interpretation of large-scale molecular data sets. *Nucleic Acids Res.* 2012;40(Database issue):D109-14 <https://doi.org/10.1093/nar/gkr988>.
58. Zhou Y, Zhou B, Pache L, Chang M, Khodabakhshi AH, Tanaseichuk O, et al. Metascape provides a biologist-oriented resource for the analysis of systems-level datasets. *Nat Commun.* 2019;10(1):1523 <https://doi.org/10.1038/s41467-019-09234-6>.
59. Maia TM, Staes A, Plasman K, Pauwels J, Boucher K, Argentini A, et al. Simple Peptide Quantification Approach for MS-Based Proteomics Quality Control. *ACS Omega.* 2020;5(12):6754-62 <https://doi.org/10.1021/acsomega.0c00080>.
60. Chiva C, Olivella R, Borràs E, Espadas G, Pastor O, Solé A, et al. QCloud: A cloud-based quality control system for mass spectrometry-based proteomics laboratories. *PLoS One.* 2018;13(1):e0189209 <https://doi.org/10.1371/journal.pone.0189209>.
61. Zhang X, Smits AH, van Tilburg GB, Ovaa H, Huber W, Vermeulen M. Proteome-wide identification of ubiquitin interactions using UbIA-MS. *Nat Protoc.* 2018;13(3):530-50 <https://doi.org/10.1038/nprot.2017.147>.
62. Ritchie ME, Phipson B, Wu D, Hu Y, Law CW, Shi W, et al. limma powers differential expression analyses for RNA-sequencing and microarray studies. *Nucleic Acids Res.* 2015;43(7):e47 <https://doi.org/10.1093/nar/gkv007>.

a**b****c**

a

